



HAL
open science

Time-domain simulation of wave propagation across resonant meta-interfaces

Marie Touboul, Bruno Lombard, Cédric Bellis

► **To cite this version:**

Marie Touboul, Bruno Lombard, Cédric Bellis. Time-domain simulation of wave propagation across resonant meta-interfaces. 2019. hal-02185076v1

HAL Id: hal-02185076

<https://hal.science/hal-02185076v1>

Preprint submitted on 16 Jul 2019 (v1), last revised 11 Apr 2020 (v2)

HAL is a multi-disciplinary open access archive for the deposit and dissemination of scientific research documents, whether they are published or not. The documents may come from teaching and research institutions in France or abroad, or from public or private research centers.

L'archive ouverte pluridisciplinaire **HAL**, est destinée au dépôt et à la diffusion de documents scientifiques de niveau recherche, publiés ou non, émanant des établissements d'enseignement et de recherche français ou étrangers, des laboratoires publics ou privés.

Time-domain simulation of wave propagation across resonant meta-interfaces

Marie Touboul^a, Bruno Lombard^{a,*}, Cédric Bellis^a

^a*Aix Marseille Univ, CNRS, Centrale Marseille, LMA UMR 7031, Marseille, France*

Abstract

Meta-interface models stem from the homogenization, in a low-frequency dynamic regime, of thin heterogeneous layers that are structured to achieve uncommon properties at the macroscopic level. When the layer is composed of a thin periodic array of highly-contrasted inclusions embedded within a homogeneous background medium then the corresponding effective interface model is characterized by jump conditions that, in the harmonic regime, involve some singular frequency-dependent terms. In this context, the article is concerned with the simulation of transient waves across such resonant meta-interfaces and a numerical method is proposed to handle the associated resonant jump conditions. To do so, a set of auxiliary variables is introduced locally along the interface and an augmented system of first-order equations in time accompanied with local-in-time jump conditions is derived. This system is then discretized on a Cartesian grid and solved using a high-order finite-difference scheme while the complexity associated with the geometry of the interface and the jump conditions is handled using an immersed interface method. A set of numerical examples in 1D and 2D is proposed to illustrate and validate the overall numerical approach, and quantitative comparisons with semi-analytical solutions are also provided.

Keywords: resonant microstructures, resonant effective interfaces, frequency-dependent jump conditions, immersed interface method, ADER scheme.

Contents

| | | |
|----------|--|----------|
| 1 | Introduction | 2 |
| 2 | Physical model | 4 |
| 2.1 | Governing equations for resonant meta-interfaces | 4 |
| 2.2 | Auxiliary variable-based time-domain formulation | 6 |
| 3 | Numerical modeling: detailed implementation in 1D | 7 |
| 3.1 | Preliminaries | 7 |
| 3.2 | ADER- K scheme | 8 |
| 3.3 | Numerical scheme at the interfaces | 8 |
| 3.4 | High-order jump conditions | 9 |

*Corresponding author. Tel.: +33 491 84 52 42 53.

Email addresses: touboul@lma.cnrs-mrs.fr (Marie Touboul), lombard@lma.cnrs-mrs.fr (Bruno Lombard), bellis@lma.cnrs-mrs.fr (Cédric Bellis)

| | | |
|-------------------|--|-----------|
| 3.5 | Computation of the phantom values | 10 |
| 3.6 | Computation of the auxiliary variables | 12 |
| 3.7 | Summary of the algorithm | 14 |
| 3.8 | Numerical analysis | 14 |
| 4 | Numerical modeling in 2D: an overview | 16 |
| 4.1 | Setting and implementation | 16 |
| 4.2 | Principal features of the implementation | 17 |
| 5 | Numerical experiments | 19 |
| 5.1 | 1D case | 19 |
| 5.2 | 2D case | 21 |
| 5.2.1 | Incident plane wave at normal incidence | 22 |
| 5.2.2 | Slanted incident plane wave on a tilted enlarged interface | 23 |
| 5.2.3 | Incident plane wave on a circular enlarged interface | 23 |
| 6 | Conclusion | 24 |
| Appendix A | Proof of Property 2 | 26 |
| Appendix A.1 | Left-side approximation of the phantom value | 26 |
| Appendix A.2 | Right-side approximation of the phantom value | 27 |
| Appendix A.3 | Local truncation error | 28 |
| Appendix B | Semi-analytical solution for a plane wave on a plane interface | 30 |
| Appendix C | Semi-analytical solution for a plane wave on a circular interface | 32 |

1. Introduction

Modeling and simulating the wave propagation within a microstructured medium can be handled efficiently by upscaling approaches such as the common homogenization methods [2, 23]. When the characteristic length-scale of the heterogeneities, which coincides with the period length in the case of periodic composite, is much smaller than a reference wavelength then the microstructure can be replaced by a homogeneous effective medium whose constitutive properties stem from those of the former. In the case where the micro-scale heterogeneities form a thin microstructured layer, see Figure 1, then dedicated homogenization methods must be employed [19] to derive effective jump conditions on an equivalent interface [21, 8, 7, 20, 4]. As a result of such a homogenization process, and owing to energy-based considerations, the heterogeneous layer is substituted by an enlarged interface, in which no calculation is performed and no field is defined but on both sides of which effective jump conditions apply. The latter depend on the material and geometrical properties of the original microstructured layer and those of the matrix.

In the case where the heterogeneous layer is composed of inclusions characterized by a large material contrast, relatively to the properties of the surrounding matrix, then illumination by an incident wave or an external source can give rise to internal resonances within the microstructure. By applying a suitable homogenization process to such a configuration, see [22], then this

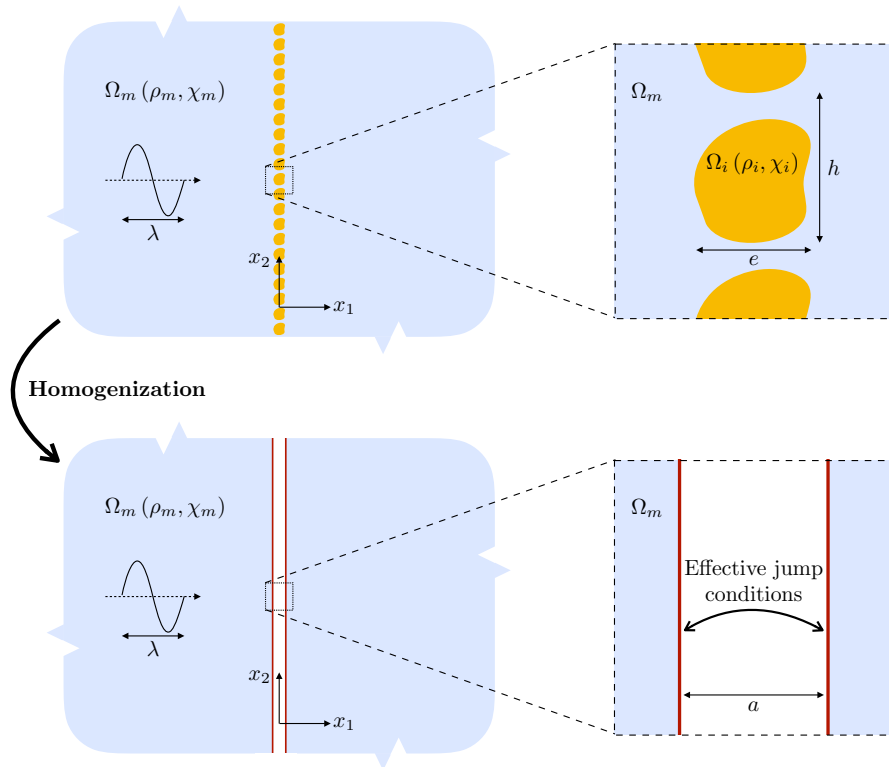


Figure 1: Homogenization process for a single periodic array of inclusions. (*top*) Original configuration with a thin microstructured layer, (*bottom*) Homogenized interface model.

phenomenon can be modeled at the macroscopic level by effective jump conditions that, in the harmonic regime, are frequency-dependent. The occurrence of such internal resonances, along with the associated homogenized models, offers new possibilities to control waves at the macroscopic level. This corresponds to the current paradigm of metamaterials and, in the present case, of resonant metasurfaces or meta-interfaces. As an example, resonant metasurfaces can be designed to optimize sound absorption [18, 24]. Exotic behaviors can also be sought and exploited, see e.g. the splitting of P- and SV-waves through elastic resonant metasurfaces [26].

In this context, the article aims at building a numerical method to simulate the interaction of transient waves with such resonant meta-interfaces. By opposition with frequency-domain approaches, time-domain formulations have two main advantages: i) they allow to simulate wide-band wave phenomena in a single computation; ii) they pave the way to problems involving nonlinearities, for which a monochromatic forcing requires to solve numerous Helmholtz equations due to the generation of harmonics. To perform such time-domain simulations, high-order finite difference schemes on uniform Cartesian grid are chosen for computational efficiency and accuracy. However, a straightforward discretization of the interfaces suffers classically from a number of drawbacks: errors of order one are introduced if the interfaces do not coincide with the mesh grid, naive stair-step discretizations yield spurious diffractions and jump conditions are not properly handled. To prevent from these drawbacks, the so-called immersed interface methods have shown to constitute efficient approaches [28]. Previous works have concerned the development of the Explicit Simplified Interface Method (ESIM) and its application to a variety of wave propagation problems [14, 6, 15, 16, 11]. In particular, simulation of time-domain

acoustic wave propagation across enlarged effective interfaces have been previously addressed in [12] but in the case of *non-resonant* effective jump conditions. In the present study, the central question therefore concerns the consideration of *resonant* effective jump conditions that are frequency-dependent in the harmonic regime along with their implementation for wave propagation simulations in the time domain.

Handling resonant meta-interfaces introduces a number of difficulties compared to the case of non-resonant interfaces. The effective jump conditions associated with the former are indeed characterized by frequency-dependent terms in the harmonic regime that yield a convolution product when transposed in the time domain. Their implementation would therefore require to store the entire history of the traces of the solution along the enlarged interface while the computation of the time convolution integral itself would substantially increase the computational cost in a naive extension of the ESIM. As a consequence, it is required to develop a specific approach to handle efficiently this type of resonant interface models numerically. For this purpose, the auxiliary variables formalism, which has been previously employed in [1] in the case of bulk dispersive metamaterials in acoustics, is adapted here to deal with the resonant meta-interfaces considered. In particular, a set of auxiliary variables is introduced locally along the enlarged interface to handle the resonant behavior of the wavefield. Due to the coupling of these additional variables with the original solution fields of the wave equation, the proposed approach involves substantial modifications of the ESIM. In counterpart, the resulting computational performances of the proposed approach is comparable with those obtained in the reference case of non-resonant interfaces.

The article is organized as follows. In Section 2, the model associated with the resonant meta-interfaces considered is presented in acoustics. The auxiliary variables formalism is then introduced and implemented to obtain an equivalent augmented system of first-order equations in time with transformed jump conditions that are local in time. Section 3 focuses in detail on a numerical implementation in 1D: the fourth-order finite-difference scheme ADER is used in combination with the ESIM. A local error analysis is performed and sufficient conditions under which a given order of accuracy can be obtained are stated. Then Section 4 provides an overview of the extension of the proposed numerical method in 2D. Numerical experiments in 1D and 2D are finally presented in Section 5, while comparisons with semi-analytical solutions allow to assess quantitatively the performance of the approach developed. Comparisons with non-resonant jump conditions are also given to investigate the effects associated with the resonant behavior of the meta-interfaces considered.

2. Physical model

2.1. Governing equations for resonant meta-interfaces

Consider the propagation of acoustic waves in a background matrix $\Omega_m \subset \mathbb{R}^2$ that contains an infinite array of inclusions Ω_i arranged periodically with a spacing h , see Figure 1. The media considered are assumed to be homogeneous and isotropic so that their constitutive parameters, being the mass density ρ and the compressibility χ , are piecewise constant:

$$\rho(\mathbf{x}) = \rho_m \mathbf{1}_{\Omega_m}(\mathbf{x}) + \rho_i \mathbf{1}_{\Omega_i}(\mathbf{x}) \quad \text{and} \quad \chi(\mathbf{x}) = \chi_m \mathbf{1}_{\Omega_m}(\mathbf{x}) + \chi_i \mathbf{1}_{\Omega_i}(\mathbf{x}) \quad (1)$$

for all $\mathbf{x} = (x_1, x_2) \in \mathbb{R}^2$ and with $\mathbf{1}_{\mathcal{D}}$ being the indicator function of a given domain \mathcal{D} . Note that the compressibility parameter χ is related to the classical wave velocity c by the relation

$\chi = (\rho c^2)^{-1}$. In the frequency-domain, the governing equations for the acoustic velocity and pressure fields, denoted as $\mathbf{v} = (v_1, v_2)$ and p respectively, read:

$$\begin{cases} i\omega \rho(\mathbf{x}) \hat{\mathbf{v}}(\mathbf{x}, \omega) = -\nabla \hat{p}(\mathbf{x}, \omega), \\ i\omega \chi(\mathbf{x}) \hat{p}(\mathbf{x}, \omega) = -\operatorname{div} \hat{\mathbf{v}}(\mathbf{x}, \omega), \end{cases} \quad (2)$$

where ω is the angular frequency and \hat{f} being the Fourier transform of a field f . Moreover, \hat{p} and $\hat{\mathbf{v}} \cdot \boldsymbol{\nu}$ are assumed to be continuous at the matrix/inclusion interfaces $\partial\Omega_i$ with normal $\boldsymbol{\nu}$. The equations (2) have to be completed with initial conditions and proper radiation conditions at infinity to ensure well-posedness. External sources terms may also be considered. Note that the system (2) is here considered in the acoustic case but it is also relevant to other physical configurations, such as linear anti-plane elasticity for which the fields \mathbf{v} , p and the parameters χ , $1/\rho$ would stand instead for stress vector, velocity, mass density and shear modulus, respectively.

In this setting and defining the background wave velocity $c_m = 1/\sqrt{\rho_m \chi_m}$, it is further assumed that the characteristic length-scale h of the microstructure is small compared to the wavelength $\lambda = 2\pi c_m/\omega$ within the matrix, i.e. $h \ll \lambda$, a condition which places the physical configuration considered in the low-frequency homogenization regime. For some values of the compressibility and the mass density, the wavelength within an inclusion is of order h . For a particular scaling between material parameters, the original problem defined above can be replaced by a resonant homogenized model that consists in a set of resonant effective jump conditions as shown in [22]. These conditions apply on an enlarged straight interface of width a , see Figure 1, and within which no calculation is performed and no field is defined. In the non-resonant case, it has been shown in [20] using an energy-based analysis that the width a of the enlarged interface must be at least equal to the width e of the microstructure. We follow the same criterion here, which leads, for an enlarged interface centered at $x_1 = 0$, to the model considered here:

$$\begin{cases} i\omega \rho_m \hat{\mathbf{v}}(\mathbf{x}, \omega) = -\nabla \hat{p}(\mathbf{x}, \omega) & (|x_1| \geq a/2, x_2 \in \mathbb{R}) \\ i\omega \chi_m \hat{p}(\mathbf{x}, \omega) = -\operatorname{div} \hat{\mathbf{v}}(\mathbf{x}, \omega) & (|x_1| \geq a/2, x_2 \in \mathbb{R}) \\ \llbracket \hat{p} \rrbracket_a = B_1 \langle \partial_1 \hat{p} \rangle_a + B_2 \langle \partial_2 \hat{p} \rangle_a & (x_2 \in \mathbb{R}) \\ \llbracket \hat{v}_1 \rrbracket_a = C_{11} \langle \partial_1 \hat{v}_1 \rangle_a + C_{12} \langle \partial_2 \hat{v}_1 \rangle_a + C_{22} \langle \partial_2 \hat{v}_2 \rangle_a + h\mathcal{D}(\omega) \langle \operatorname{div} \hat{\mathbf{v}} \rangle_a & (x_2 \in \mathbb{R}), \end{cases} \quad (3)$$

where $\partial_j \cdot = \frac{\partial \cdot}{\partial x_j}$ while

$$\llbracket f(\mathbf{x}) \rrbracket_a = f(a/2, x_2) - f(-a/2, x_2), \quad \langle f(\mathbf{x}) \rangle_a = \frac{1}{2} (f(a/2, x_2) + f(-a/2, x_2)) \quad (4)$$

denote the jump and the mean value of a given field f relatively to the enlarged interface, respectively. In addition, the constitutive parameters B_1 , B_2 , C_{11} , C_{12} and C_{22} featured in (3) depend only on the geometry of the inclusions Ω_i and on the material parameters of the matrix and inclusions. Moreover, the term $\mathcal{D}(\omega)$ is a frequency-dependent parameter that encapsulates the resonant behavior of the inclusions. Remarkably, this term can be expanded as:

$$\mathcal{D}(\omega) = \alpha_0 - \sum_{r \geq 1} \alpha_r^2 \frac{\omega^2}{\omega^2 - \omega_r^2}, \quad (5)$$

where $\{\omega_r\}_{r \geq 1}$ is a set of resonant frequencies associated with real-valued coefficients $\{\alpha_r\}_{r \geq 0}$. Note that the non-resonant effective interface model considered in [12] can formally be recovered by setting $\alpha_r = 0$ for all $r \geq 0$. Lastly, with the purpose of simulating transient waves using the above meta-interface model, we assume that the sum in (5) can be truncated to a finite number N_R of resonances based on the analysis of the frequency content of a given illuminating wave.

Remark 1. *The derivation of the effective model is beyond the scope of the present study and the model (3) will be considered as such to perform wave propagation simulations hereafter. In particular, the featured constitutive parameters will be chosen independently of a microstructure. Moreover, even if the effective jump conditions are obtained [22] for configurations with zero curvature, they will be employed in Section 4 for 2D configurations involving curved enlarged interfaces as well. In this case, they will be properly expressed using a curvilinear coordinates system.*

2.2. Auxiliary variable-based time-domain formulation

Owing to the frequency dependence of the term $\mathcal{D}(\omega)$ in (5), then the transposition of the system (3) to the time domain brings up a convolution integral in time. Handling numerically such a non-local term is very costly and would therefore reduce the computational gains associated with the treatment of the microstructured layer through an effective model.

To circumvent this difficulty, the auxiliary variable approach can be used to obtain a set of equations in a local form, see [1] for the application of the latter to dispersive metamaterials in bulk. Accordingly, let define locally on the enlarged interface, the so-called auxiliary variables \hat{J}_r and \hat{G}_r , which are associated with the resonance index $r \in \{1, \dots, N_R\}$ and satisfy the following equations:

$$\begin{cases} (\omega^2 - \omega_r^2)\hat{J}_r(x_2, \omega) = \alpha_r^2 \omega^2 \langle \text{div } \hat{\mathbf{v}}(\mathbf{x}, \omega) \rangle_a & \text{for } x_2 \in \mathbb{R}. \\ i\omega \hat{J}_r(x_2, \omega) = \hat{G}_r(x_2, \omega) \end{cases} \quad (6)$$

Setting $\tilde{C}_{11} = C_{11} + h\alpha_0$ and $\tilde{C}_{22} = C_{22} + h\alpha_0$ while combining (3) and (6) then yields the following system in the time domain for all $t > 0$ by a formal application of the inverse Fourier transform:

$$\begin{cases} \partial_t \mathbf{v}(\mathbf{x}, t) = -\frac{1}{\rho_m} \nabla p(\mathbf{x}, t) & (|x_1| \geq a/2, x_2 \in \mathbb{R}) \\ \partial_t p(\mathbf{x}, t) = -\frac{1}{\chi_m} \text{div } \mathbf{v}(\mathbf{x}, t) & (|x_1| \geq a/2, x_2 \in \mathbb{R}) \\ \partial_t G_r(x_2, t) = -\omega_r^2 J_r(x_2, t) + (c_m \alpha_r)^2 \langle \Delta \text{div } \mathbf{v}(\mathbf{x}, t) \rangle_a & (x_2 \in \mathbb{R}, r = 1, \dots, N_R) \\ \partial_t J_r(x_2, t) = G_r(x_2, t) & (x_2 \in \mathbb{R}, r = 1, \dots, N_R) \\ \llbracket p \rrbracket_a = B_1 \langle \partial_1 p \rangle_a + B_2 \langle \partial_2 p \rangle_a & (x_2 \in \mathbb{R}) \\ \llbracket v_1 \rrbracket_a = \tilde{C}_{11} \langle \partial_1 v_1 \rangle_a + C_{12} \langle \partial_2 v_1 \rangle_a + \tilde{C}_{22} \langle \partial_2 v_2 \rangle_a - h \sum_{r=1}^{N_R} J_r & (x_2 \in \mathbb{R}). \end{cases} \quad (7)$$

Note that, consistently the definition (6), the auxiliary variables J_r are not averaged in the last equation of the above system.

Remark 2. The auxiliary variables $\{\hat{J}_r\}$ are defined through (6) for all $\omega \neq \omega_r$. Therefore, in order to apply the inverse Fourier transform, care must be taken and a suitable approach relies on the introduction of an artificial damping parameter that is taken to zero once in the time domain. Studying such a limit amounts to investigate the question of the existence of a limiting absorption principle for the system considered, which is however beyond the scope of this work. Reference can be made to, e.g., [5] for the treatment of this question for dispersive media in electromagnetism.

Starting from the original variable set $\mathbf{u} = (p, \mathbf{v})^\top$, the set $\mathbf{w} = (\{J_r\}, \{G_r\})^\top$ of auxiliary variables is introduced locally along the enlarged interface to allow the derivation of the system (7). The latter consists of first-order equations in time that are complemented by jump conditions that are local in time. Considering the complete set of variables $\tilde{\mathbf{u}} = (\mathbf{u}, \mathbf{w})^\top$ then (7) can be written in a compact form for all $t > 0$ as:

$$\begin{cases} \partial_t \mathbf{u} + \mathbb{A}_j \partial_j \mathbf{u} = \mathbf{0} & (|x_1| \geq a/2, x_2 \in \mathbb{R}), \\ \partial_t \mathbf{w} + \mathbb{B} \langle \partial_j^2 \partial_\ell \mathbf{u} \rangle_a + \mathbb{C} \mathbf{w} = \mathbf{0} & (x_2 \in \mathbb{R}), \\ \llbracket \mathbf{u} \rrbracket_a = \mathbb{D}_j \langle \partial_j \mathbf{u} \rangle_a + \mathbb{E} \mathbf{w} & (x_2 \in \mathbb{R}), \end{cases} \quad (8)$$

using the Einstein summation convention for repeated indices and where the matrices \mathbb{A}_j , \mathbb{B} , \mathbb{C} , \mathbb{D}_j and \mathbb{E} concatenate the parameters characterizing the resonant meta-interface model considered.

3. Numerical modeling: detailed implementation in 1D

3.1. Preliminaries

In this section, we describe the numerical implementation of the system (7) in a one-dimensional configuration which is representative of the propagation of a plane wave illuminating a straight enlarged interface at normal incidence in 2D. The velocity reduces to the scalar field $\mathbf{v}(\mathbf{x}) = v(x) \mathbf{e}_1$ where $x = \mathbf{x} \cdot \mathbf{e}_1$ with $(\mathbf{e}_1, \mathbf{e}_2)$ being the canonical basis of \mathbb{R}^2 . In this setting, the system (7) is recast for all $t > 0$ as:

$$\begin{cases} \partial_t v(x, t) = -\frac{1}{\rho_m} \partial_x p(x, t) & (|x_1| \geq a/2), & (9a) \\ \partial_t p(x, t) = -\frac{1}{\chi_m} \partial_x v(x, t) & (|x_1| \geq a/2), & (9b) \\ \partial_t G_r(t) = -\omega_r^2 J_r(t) + (c_m \alpha_r)^2 \langle \partial_x^3 v(x, t) \rangle_a & (r = 1, \dots, N_R), & (9c) \\ \partial_t J_r(t) = G_r(t) & (r = 1, \dots, N_R), & (9d) \\ \llbracket p(x, t) \rrbracket_a = B_1 \langle \partial_x p(x, t) \rangle_a, & & (9e) \\ \llbracket v(x, t) \rrbracket_a = \tilde{C}_{11} \langle \partial_x v(x, t) \rangle_a - h \sum_{r=1}^{N_R} J_r(t). & & (9f) \end{cases}$$

According to the condensed form (8), we introduce the matrix

$$\mathbb{A} = \begin{pmatrix} 0 & 1/\chi_m \\ 1/\rho_m & 0 \end{pmatrix} \quad (10)$$

so that summing up (9a) and (9b) yields

$$\partial_t \mathbf{u} + \mathbb{A} \partial_x \mathbf{u} = \mathbf{0} \quad (|x_1| \geq a/2). \quad (11)$$

3.2. ADER- K scheme

The solution \mathbf{u} is discretized with a mesh size Δx and a time step Δt . We denote as \mathbf{u}_i^n the approximation of \mathbf{u} at the point $x_i = i\Delta x$ and time $t_n = n\Delta t$. The explicit finite-difference ADER- K scheme [25, 17], with K an even integer, is used to solve numerically (11). When applied to an equation such as (11) in a homogeneous domain, this scheme is of order K in both space and time for sufficiently smooth initial data and, for $K = 4$, it is stable under the CFL condition $\Delta t \leq \Delta x/c_m$. Its time-marching scheme writes:

$$\mathbf{u}_i^{n+1} = \mathbf{u}_i^n - \sum_{s=-K/2}^{+K/2} \sum_{m=1}^K \nu_{K,m,s} \left(\frac{\Delta t}{\Delta x} \mathbb{A} \right)^m \mathbf{u}_{i+s}^n, \quad (12)$$

where the $\nu_{K,m,s}$ are a set of coefficients such that, if the solution \mathbf{u} is of class C^K , then its m -th order derivative can be approximated as [11]:

$$\partial_x^m \mathbf{u}(x_j, t_n) = \frac{(-1)^{m+1}}{\Delta x^m} m! \sum_{s=-K/2}^{K/2} \nu_{K,m,s} \mathbf{u}(x_{j+s}, t_n) + \mathcal{O}(\Delta x^{K+1}), \quad m = 0, \dots, K. \quad (13)$$

Inserting Taylor expansions for $\mathbf{u}(x_{j+s}, t_n)$ at (x_j, t_n) and up to the order K in the previous expression leads to the following relations that are satisfied by the coefficients $\nu_{K,m,s}$ for $0 \leq k, m \leq K$:

$$\sum_{s=-K/2}^{K/2} \nu_{K,m,s} s^k = \begin{cases} (-1)^{m+1} & \text{if } k = m \\ 0 & \text{else.} \end{cases} \quad (14)$$

For now on, we choose the ADER scheme with $K = 4$ which we consider to allow a good compromise between accuracy and ease of implementation.

3.3. Numerical scheme at the interfaces

Considering the time-marching scheme (12), two types of points can be distinguished, see Figure 2: (i) *regular points* that are the grid nodes for which the stencil does not intersect the enlarged interface, and (ii) *irregular points* that are the nodes whose stencil includes at least one node within the enlarged interface where the solution is actually not defined. Such grid nodes x_i lying within the enlarged interface are referred to as *phantom points*. For time-marching at the irregular points, the scheme (12) is modified: *phantom values* \mathbf{u}^* have to be defined and used at the phantom points x_i within the enlarged interface while standard numerical values can be used otherwise. In the framework of the Explicit Simplified Interface Method (ESIM), these phantom values are defined as smooth extrapolations of the solution at the phantom points from the values of the solution at the physical points $\pm a/2$. In the case of the ADER-4 scheme, they are given by

$$\begin{cases} \mathbf{u}^*(x_i, t_n) = \sum_{m=0}^q \frac{1}{m!} \left(x_i + \frac{a}{2} \right)^m \partial_x^m \mathbf{u} \left(-\frac{a}{2}, t_n \right) & \text{for } i = I_L + 1, I_L + 2, \\ \mathbf{u}^*(x_i, t_n) = \sum_{m=0}^q \frac{1}{m!} \left(x_i - \frac{a}{2} \right)^m \partial_x^m \mathbf{u} \left(\frac{a}{2}, t_n \right) & \text{for } i = I_R - 1, I_R - 2, \end{cases} \quad (15)$$

where I_L and I_R are the indices of the grid nodes that are the closest to the enlarged interface on each side and $q > 1$ is a user-chosen parameter that controls the accuracy of the approximation.

Remark 3. Note that in the definition (15) of the phantom values, the point x_i is a grid node that is situated in the enlarged interface while $\pm a/2$ is a physical point that may not coincide with a grid node. This is the whole point of the ESIM, which allows to implement jump conditions at interfaces whose geometry may be independent of the computational grid of the finite-difference scheme considered.

This methodology has been implemented in the case of non-resonant effective interface models in [12]. It is extended here to the case of resonant models, which requires substantial modifications due to use of auxiliary variables. In the sections 3.4 and 3.5, it is shown how the computation of the phantom values through (15) rely both on the use of the jump conditions (9e-9f) and on Taylor expansions on both sides of the enlarged interface.

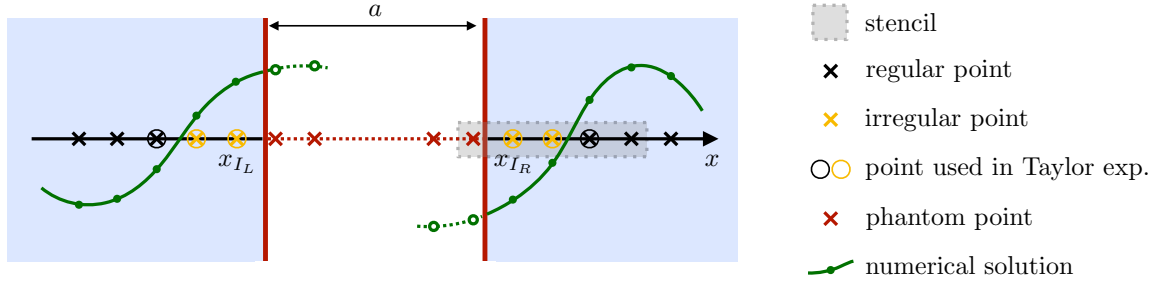


Figure 2: Nodes surrounding the enlarged interface for the ADER-4 scheme.

3.4. High-order jump conditions

The phantom values \mathbf{u}^* in (15) are expressed in terms of the spatial derivatives $\partial_x^m \mathbf{u}$ at $\pm a/2$. To compute the latter, one is required to derive q -th order jump conditions relating the traces of the spatial derivatives of the solution, up to its q -th derivative. Some notations are introduced: the vectors $\mathbf{U}_+^q(t_n)$ and $\mathbf{U}_-^q(t_n)$ concatenate $q_U = (2q + 2)$ unknowns which are the traces of the spatial derivatives of the fields p and v up to order q and on each side as

$$\mathbf{U}_\pm^q(t_n) = (p_\pm(t_n), \partial_x p_\pm(t_n), \dots, \partial_x^q p_\pm(t_n), v_\pm(t_n), \partial_x v_\pm(t_n), \dots, \partial_x^q v_\pm(t_n))^\top \in \mathbb{R}^{q_U}, \quad (16)$$

where $p_\pm(t_n) \equiv p(\pm a/2, t_n)$ and $v_\pm(t_n) \equiv v(\pm a/2, t_n)$ and employing the same notation for the spatial derivatives. Moreover, the vector \mathbf{Z} contains the $2N_R$ auxiliary variables at time t_n , i.e.

$$\mathbf{Z}(t_n) = (J_1(t_n), \dots, J_{N_R}(t_n), G_1(t_n), \dots, G_{N_R}(t_n))^\top \in \mathbb{R}^{2N_R}. \quad (17)$$

To obtain jump conditions at the order q , i.e. a relation between the vectors \mathbf{U}_+^q , \mathbf{U}_-^q and \mathbf{Z} , the zero-th order jump conditions (9e) and (9f) are first differentiated in time and the equations (9a) and (9b) are used to replace time derivatives by spatial derivatives. This yields a relation between the vectors \mathbf{U}_+^1 , \mathbf{U}_-^1 and \mathbf{Z} . This process of differentiating in time the jump conditions is iterated up to the chosen value of the parameter q while the equation (9c) is used to express the term $\partial_t G_r$ using J_r and $\langle \partial_x^3 v \rangle_a$ when necessary. The q -th order jump conditions so obtained are written as:

$$\mathbb{C}_+^q \mathbf{U}_+^q(t_n) + \mathbf{R}_+^q(t_n) = \mathbb{C}_-^q \mathbf{U}_-^q(t_n) + \mathbf{R}_-^q(t_n) + \mathbb{Q}^q \mathbf{Z}(t_n), \quad (18)$$

with \mathbb{C}_\pm^q being $q_U \times q_U$ matrices that depend only on the interface parameters and \mathbb{Q}^q is a $q_U \times 2N_R$ matrix that depends only on the physical parameters and on the resonant frequencies. The q_U -element vectors $\mathbf{R}_\pm^q(t_n)$ contain the $(q+1)$ -th order derivatives of p and v .

In the ensuing numerical examples, the values $q = 3$ and $q = 5$ are chosen and it is checked numerically that the corresponding matrices \mathbb{C}_\pm^q are invertible. In the case $q = 3$ the entries of the above matrices are given below:

$$\begin{cases} \mathbb{C}_\pm^3[i, i] = 1, & \mathbb{C}_\pm^3[5, 6] = \mp \frac{\tilde{C}_{11}}{2}, \\ \mathbb{C}_\pm^3[1, 2] = \mp \frac{B_1}{2}, & \mathbb{C}_\pm^3[6, 7] = \mp \frac{B_1}{2}, \\ \mathbb{C}_\pm^3[2, 3] = \mp \frac{\tilde{C}_{11}}{2}, & \mathbb{C}_\pm^3[7, 8] = \mp \frac{1}{2} \left(\tilde{C}_{11} - h \sum_{r=1}^{N_R} \alpha_r^2 \right), \\ \mathbb{C}_\pm^3[3, 4] = \mp \frac{B_1}{2}, & \mathbb{C}_\pm^3[i, j] = 0 \text{ else.} \end{cases} \quad (19)$$

$$\begin{cases} \mathbb{Q}^3[2, j] = h\rho_m & \text{if } j \in \{N_R + 1, \dots, 2N_R\}, & \mathbb{Q}^3[7, j] = \frac{h\omega_j^2}{c^2} & \text{if } j \in \{1, \dots, N_R\}, \\ \mathbb{Q}^3[4, j] = -\frac{h\rho_m\omega_{j-N_R}^2}{c_m^2} & \text{if } j \in \{N_R + 1, \dots, 2N_R\}, & \mathbb{Q}^3[i, j] = 0 & \text{else.} \\ \mathbb{Q}^3[5, j] = -h & \text{if } j \in \{1, \dots, N_R\}, \end{cases} \quad (20)$$

$$\begin{cases} \mathbf{R}_\pm^3[4] = \mp \frac{B_1}{2} \partial_x^4 v_\pm, & \mathbf{R}_\pm^3[8] = \mp \frac{1}{2} \left(\tilde{C}_{11} - h \sum_{r=1}^{N_R} \alpha_r^2 \right) \partial_x^4 p_\pm, & \mathbf{R}_\pm^3[i] = 0 \text{ else.} \end{cases} \quad (21)$$

3.5. Computation of the phantom values

Consider $\mathbb{T}_i^q(\pm a/2)$ as the $2 \times q_U$ matrices of the polynomial forms of the Taylor expansions at the order q between the grid node with index i and the physical point $\pm a/2$, which may not coincide with a grid point, see Remark 3, i.e.

$$\mathbb{T}_i^q(\pm a/2) = \begin{pmatrix} 1 & (x_i \pm a/2) & \dots & (x_i \pm a/2)^q/q! & 0 & 0 & \dots & 0 \\ 0 & 0 & \dots & 0 & 1 & (x_i \pm a/2) & \dots & (x_i \pm a/2)^q/q! \end{pmatrix}.$$

Using the q -th order jump conditions (18) and as the matrix \mathbb{C}_\pm^q is invertible in the cases considered hereafter, the equation (15) can now be recast as

$$\begin{cases} \mathbf{u}^*(x_i, t_n) = \mathbb{T}_i^q\left(-\frac{a}{2}\right) \mathbf{U}_-^q(t_n) & \text{for } i = I_L + 1, I_L + 2, \\ \mathbf{u}^*(x_i, t_n) = \mathbb{T}_i^q\left(\frac{a}{2}\right) (\mathbb{C}_+^q)^{-1} [\mathbb{C}_-^q \mathbf{U}_-^q(t_n) + \mathbb{Q}^q \mathbf{Z}(t_n) + \mathbf{R}_-^q(t_n) - \mathbf{R}_+^q(t_n)] & \text{for } i = I_R - 1, I_R - 2. \end{cases} \quad (22)$$

Now, to determine $\mathbf{U}_-^q(t_n)$ we introduce a user-chosen parameter q_T according to which Taylor expansions are written out at the q_T nodes $x_i = x_{I_L - q_T + 1}, \dots, x_{I_L}$ on the left side of the enlarged interface as

$$\mathbf{u}(x_i, t_n) = \mathbb{T}_i^q\left(-\frac{a}{2}\right) \mathbf{U}_-^q(t_n) + \mathcal{O}(\Delta x^{q+1}), \quad (23)$$

and at the q_T nodes $x_i = x_{I_R}, \dots, x_{I_R+q_T-1}$ on the right side of the enlarged interface as

$$\begin{aligned} \mathbf{u}(x_i, t_n) &= \mathbb{T}_i^q \left(\frac{a}{2} \right) \mathbf{U}_+^q(t_n) + \mathcal{O}(\Delta x^{q+1}) \\ &= \mathbb{T}_i^q \left(\frac{a}{2} \right) (\mathbb{C}_+^q)^{-1} [\mathbb{C}_-^q \mathbf{U}_-^q(t_n) + \mathbb{Q}^q \mathbf{Z}(t_n) + \mathbf{R}_-^q(t_n) - \mathbf{R}_+^q(t_n)] + \mathcal{O}(\Delta x^{q+1}) \end{aligned} \quad (24)$$

where we made use of (18) and, by an abuse of notations, the term $\mathcal{O}(\Delta x^{q+1})$ denotes a vector with entries of the order of Δx^{q+1} and whose size may vary from line to line. Introducing the $4q_T$ -element vectors $\mathbf{u}(t_n)$ and $\mathbf{\Delta}(t_n)$ by blocks as

$$\mathbf{u}(t_n) = \begin{pmatrix} \mathbf{u}(x_{I_L-q_T+1}, t_n) \\ \vdots \\ \mathbf{u}(x_{I_L}, t_n) \\ \mathbf{u}(x_{I_R}, t_n) - \mathbb{T}_{I_R}^q \left(\frac{a}{2} \right) (\mathbb{C}_+^q)^{-1} \mathbb{Q}^q \mathbf{Z}(t_n) \\ \vdots \\ \mathbf{u}(x_{I_R+q_T-1}, t_n) - \mathbb{T}_{I_R+q_T-1}^q \left(\frac{a}{2} \right) (\mathbb{C}_+^q)^{-1} \mathbb{Q}^q \mathbf{Z}(t_n) \end{pmatrix}, \quad (25)$$

$$\mathbf{\Delta}(t_n) = \begin{pmatrix} \mathbf{0} \\ \vdots \\ \mathbf{0} \\ \mathbb{T}_{I_R}^q \left(\frac{a}{2} \right) (\mathbb{C}_+^q)^{-1} (\mathbf{R}_-^q(t_n) - \mathbf{R}_+^q(t_n)) \\ \vdots \\ \mathbb{T}_{I_R+q_T-1}^q \left(\frac{a}{2} \right) (\mathbb{C}_+^q)^{-1} (\mathbf{R}_-^q(t_n) - \mathbf{R}_+^q(t_n)) \end{pmatrix}, \quad (26)$$

and the $4q_T \times q_U$ matrix \mathbb{M} as

$$\mathbb{M} = \begin{pmatrix} \mathbb{T}_{I_L-q_T+1}^q \left(-\frac{a}{2} \right) \\ \vdots \\ \mathbb{T}_{I_L}^q \left(-\frac{a}{2} \right) \\ \mathbb{T}_{I_R}^q \left(\frac{a}{2} \right) (\mathbb{C}_+^q)^{-1} \mathbb{C}_-^q \\ \vdots \\ \mathbb{T}_{I_R+q_T-1}^q \left(\frac{a}{2} \right) (\mathbb{C}_+^q)^{-1} \mathbb{C}_-^q \end{pmatrix}, \quad (27)$$

then, from (23) and (24) one obtains the following system:

$$\mathbb{M} \mathbf{U}_-^q(t_n) = \mathbf{u}(t_n) - \mathbf{\Delta}(t_n) + \mathcal{O}(\Delta x^{q+1}). \quad (28)$$

When the parameter q_T is chosen as $4q_T = q_U$, then \mathbb{M} is a square matrix that is formally checked to be invertible. If $4q_T > q_U$ then \mathbb{M} is not square and, in such a case, we denote by \mathbb{M}^{-1} its Moore-Penrose pseudo-inverse. Therefore, we arrive at the following expressions for the phantom values, for $i = I_L + 1, I_L + 2$:

$$\mathbf{u}^*(x_i, t_n) = \mathbb{T}_i^q \left(-\frac{a}{2} \right) \mathbb{M}^{-1} (\mathbf{u}(t_n) - \mathbf{\Delta}(t_n) + \mathcal{O}(\Delta x^{q+1})), \quad (29)$$

and for $i = I_R - 2, I_R - 1$:

$$\mathbf{u}^*(x_i, t_n) = \mathbb{T}_i^q \left(\frac{a}{2} \right) (\mathbb{C}_+^q)^{-1} [\mathbb{C}_-^q \mathbb{M}^{-1} (\mathbf{u}(t_n) - \mathbf{\Delta}(t_n) + \mathcal{O}(\Delta x^{q+1})) + \mathbb{Q}^q \mathbf{Z}(t_n) + \mathbf{R}_-^q(t_n) - \mathbf{R}_+^q(t_n)]. \quad (30)$$

Neglecting some terms in (29) and (30) then allows us to formulate the approximation below.

Approximation 1. *The numerical approximations $(\mathbf{u}^*)_i^n$ of the phantom values $\mathbf{u}^*(x_i, t_n)$ are computed using the formulae*

$$\begin{cases} (\mathbf{u}^*)_i^n = \mathbb{T}_i^q \left(-\frac{a}{2} \right) \mathbb{M}^{-1} \mathbf{u}^n & \text{for } i = I_L + 1, I_L + 2, \\ (\mathbf{u}^*)_i^n = \mathbb{T}_i^q \left(\frac{a}{2} \right) (\mathbb{C}_+^q)^{-1} [\mathbb{C}_-^q \mathbb{M}^{-1} \mathbf{u}^n + \mathbb{Q}^q \mathbf{Z}^n] & \text{for } i = I_R - 2, I_R - 1, \end{cases} \quad (31)$$

in terms of the numerical approximations \mathbf{u}^n , \mathbf{Z}^n of $\mathbf{u}(t_n)$, $\mathbf{Z}(t_n)$, respectively.

The quality of this approximation is analyzed in [Appendix A](#) through a local truncation error analysis. In practice, the matrices $\mathbb{T}_i^q(\pm \frac{a}{2})$, \mathbb{C}_\pm^q and \mathbb{M}^{-1} featured in (31) are computed in a pre-processing step once for all.

3.6. Computation of the auxiliary variables

The computation of the phantom values \mathbf{u}^* through [Approximation 1](#) requires to determine an approximation \mathbf{Z}^n of the vector $\mathbf{Z}(t_n)$ of auxiliary variables (17) at each time step. Assuming zero initial conditions for J_r and G_r , which is justified in the case where the enlarged interface is illuminated by a remote source, then integrating (9c-9d) yields

$$\begin{cases} J_r(t_n) = \Lambda_r^1(t_n) \cos(\omega_r t_n) - \Lambda_r^2(t_n) \sin(\omega_r t_n), \\ G_r(t_n) = -\omega_r (\Lambda_r^2(t_n) \cos(\omega_r t_n) + \Lambda_r^1(t_n) \sin(\omega_r t_n)), \end{cases} \quad (32)$$

where, owing to (9a-9b), one has for $i = 1, 2$:

$$\Lambda_r^i(t_n) = \frac{\alpha_r^2}{\omega_r \rho_m} \int_0^{t_n} \ell_r^i(\tau) d\tau \quad \text{with} \quad \begin{cases} \ell_r^1(\tau) = \partial_t \langle \partial_x^2 p \rangle_a(\tau) \sin(\omega_r \tau), \\ \ell_r^2(\tau) = \partial_t \langle \partial_x^2 p \rangle_a(\tau) \cos(\omega_r \tau). \end{cases} \quad (33)$$

In practice, the functions Λ_r^i in (33) are computed iteratively as

$$\begin{cases} \Lambda_r^i(t_0) = 0, \\ \Lambda_r^i(t_n) = \Lambda_r^i(t_{n-1}) + \frac{\alpha_r^2}{\omega_r \rho_m} \int_{t_{n-1}}^{t_n} \ell_r^i(\tau) d\tau, \end{cases} \quad (34)$$

where $t_0 = 0$ and the integral is computed using the extrapolative Newton-Cotes formulas [27], i.e.

$$\int_{t_{n-1}}^{t_n} \ell_r^i(\tau) d\tau = \Delta t \sum_{m=0}^{q_I-2} \gamma_m \ell_r^i(t_{n-1-m}) + \mathcal{O}(\Delta t^{q_I}). \quad (35)$$

The values of the parameters γ_m for $q_I = 2, \dots, 5$ are reported in [Table 1](#).

| q_I | 2 | 3 | 4 | 5 |
|------------|---|------|--------|--------|
| γ_0 | 1 | 3/2 | 23/12 | 55/24 |
| γ_1 | | -1/2 | -16/12 | -59/24 |
| γ_2 | | | 5/12 | 37/24 |
| γ_3 | | | | -9/24 |

Table 1: Numerical integration by the Newton-Cotes formulas: values of the parameter γ_m featured in (35).

| q_D | 1 | 2 | 3 | 4 |
|-----------|----|------|-------|---------|
| β_0 | 1 | 3/2 | 11/6 | 75/36 |
| β_1 | -1 | -4/2 | -18/6 | -144/36 |
| β_2 | | 1/2 | 9/6 | 108/36 |
| β_3 | | | -2/6 | -48/36 |
| β_4 | | | | 9/36 |

Table 2: Numerical derivation: values of the parameter β_w featured in (36).

Moreover, the computation of the terms $\ell_r^i(t_{n-1-m})$ defined through in (33) and used in (35) requires to approximate the temporal derivative $\partial_t \langle \partial_x^2 p \rangle_a(t_{n-1-m})$, which is achieved using the following finite-difference approximation:

$$\partial_t \langle \partial_x^2 p \rangle_a(t_{n-1-m}) = \frac{1}{\Delta t} \sum_{w=0}^{q_D} \beta_w \langle \partial_x^2 p \rangle_a(t_{n-1-m-w}) + \mathcal{O}(\Delta t^{q_D}). \quad (36)$$

The values of β_w for $q_D = 1, \dots, 4$ are listed in Table 2.

Remark 4. Owing to (9c), the term $\langle \partial_x^3 v \rangle_a$ can be used in (33) instead of the quantity $\partial_t \langle \partial_x^2 p \rangle_a$ with mixed derivatives in time and space. However, in practice, numerical instabilities have been observed in 2D when the third-order spatial derivative is used, contrary to the mixed approach described here. Such instabilities were not observed in 1D but we adopt this mixed approach for the 1D case as well for consistency.

By inserting (35) and (36) in (34), while keeping track of the approximation order, we finally arrive at the following approximation.

Approximation 2. The numerical approximation $(\Lambda_r^i)^n$ of $\Lambda_r^i(t_n)$ for $i = 1, 2$ is computed by the recurrence relation

$$\begin{cases} (\Lambda_r^i)^0 = 0, \\ (\Lambda_r^i)^n = (\Lambda_r^i)^{n-1} + \frac{\alpha_r^2}{\omega_r \rho_m} \sum_{m=0}^{q_I-2} \gamma_m \sum_{w=0}^{q_D} \beta_w (\langle \partial_x^2 p \rangle_a)^{n-1-m-w} (\kappa_r^i)^{n-1-m-w} \end{cases} \quad (37)$$

with $(\kappa_r^1)^s = \sin(\omega_r t_s)$ and $(\kappa_r^2)^s = \cos(\omega_r t_s)$ while $(\langle \partial_x^2 p \rangle_a)^s$ denotes the numerical approximation of $\langle \partial_x^2 p \rangle_a(t_s)$. The numerical counterpart $\mathbf{Z}^n = (\{J_r^n\}, \{G_r^n\})$ of the auxiliary variables vector $\mathbf{Z}(t_n) = (\{J_r(t_n)\}, \{G_r(t_n)\})$ at the time step t_n is then computed by:

$$\begin{cases} J_r^n = (\Lambda_r^1)^n \cos(\omega_r t_n) - (\Lambda_r^2)^n \sin(\omega_r t_n), \\ G_r^n = -\omega_r ((\Lambda_r^2)^n \cos(\omega_r t_n) + (\Lambda_r^1)^n \sin(\omega_r t_n)), \end{cases} \quad (38)$$

Property 1. *Approximation 2 satisfies the following estimates:*

$$\begin{cases} J_r(t_n) = J_r^n + \mathcal{O}(\Delta t^{q_D+2}) + \mathcal{O}(\Delta t^{q_I}), \\ G_r(t_n) = G_r^n + \mathcal{O}(\Delta t^{q_D+1}) + \mathcal{O}(\Delta t^{q_I}). \end{cases} \quad (39)$$

In practice, owing to the formula (37), the computation of the auxiliary variables J_r^n, G_r^n at a given time step t_n only requires the knowledge of $(\Lambda_r^1)^{n-1}, (\Lambda_r^2)^{n-1}$ and $(\langle \partial_x^2 p \rangle_a)^{n-1-m-w}$ for $m = 0, \dots, (q_I - 2)$ and $w = 0, \dots, q_D$. These quantities constitute a set of memory variables, which we regroup in the following vector

$$\Psi^n = ((\Lambda_r^1)^{n-1}, (\Lambda_r^2)^{n-1}, \{(\langle \partial_x^2 p \rangle_a)^{n-1-m-w}\}_{m,w})^\top, \quad (40)$$

of size $(q_D + 1) \times (q_I - 1) + 2$. The terms $(\langle \partial_x^2 p \rangle_a)^{n-1-m-w}$ in (40) are computed from the numerical approximations of \mathbf{U}_-^q and \mathbf{U}_+^q using (28) and (18), respectively, at each time step. The vector Ψ^n is stored and updated during the entire simulation.

3.7. Summary of the algorithm

Algorithm 1 Time-marching scheme with auxiliary variables and phantom values

I. Pre-processing:

1. Detection of the irregular points surrounding the enlarged interface.
2. Computation of the matrices $\mathbb{M}^{-1}, \mathbb{C}_-^q, (\mathbb{C}_+^q)^{-1}$ and \mathbb{Q}^q .
3. Computation of $\mathbb{T}_i^q(-\frac{a}{2})\mathbb{M}^{-1}$ for phantom values at the left side of the enlarged interface.
4. Computation of $\mathbb{T}_i^q(\frac{a}{2})(\mathbb{C}_+^q)^{-1}\mathbb{C}_-^q\mathbb{M}^{-1}$ and $\mathbb{T}_i^q(\frac{a}{2})(\mathbb{C}_+^q)^{-1}\mathbb{Q}^q$ for phantom values at the right side of the enlarged interface.

II. *Initialization:* set the solution \mathbf{u}_i^0 at $t_0 = 0$ while $\Psi^0 = \mathbf{0}$ along the enlarged interface.

III. Iterate in time $n \geq 0$:

1. Computation of the auxiliary variables vector \mathbf{Z}^n from Ψ^n using Approximation 2.
 2. Computation of \mathbf{u}^n in (25) from \mathbf{u}_i^n and \mathbf{Z}^n .
 3. Computation of the phantom values $(\mathbf{u}^*)^n_i$ using Approximation 1.
 4. Time-marching using (12) to compute the solution \mathbf{u}_i^{n+1} for all i with the phantom values being used where necessary.
 5. Update of the memory variables vector Ψ^{n+1} in (40).
-

3.8. Numerical analysis

To the Authors' knowledge, there is no theoretical result available on the numerical stability of the ESIM. In the non-resonant case, no stability issue has been observed on a large number of

simulations that involved interfaces with various constitutive parameters and positions within the finite-difference grid [12]. In the resonant case considered in the present study, the stability is observed in practice to depend on the order of integration q_I in (35), on the order of derivation q_D in (36) on and the number q_T of grid nodes considered for the Taylor expansions (23-24). In practice, given (q_D, q_I) , the stability is observed on numerical experiments for the minimal values of q_T that are reported in Table 3. The case $(q_D, q_I) = (4, 5)$ is not reported because q_T being too large, the use of the pseudo-inverse of the associated matrix \mathbb{M} yields unacceptable numerical errors. When q_T is chosen according to Table 3, then the CFL condition $\Delta t \leq \Delta x/c_m$ of the ADER-4 scheme in a homogeneous domain seems to be the critical threshold for stability here as well.

| $q_D \backslash q_I$ | 2 | 3 | 4 | 5 |
|----------------------|---------|-------------|-------------|-------------|
| 1 | $q_U/4$ | $q_U/4$ | $q_U/4$ | $q_U/4$ |
| 2 | $q_U/4$ | $q_U/4 + 1$ | $q_U/4 + 1$ | $q_U/4 + 1$ |
| 3 | $q_U/4$ | $q_U/4 + 1$ | $q_U/4 + 2$ | $q_U/4 + 2$ |
| 4 | $q_U/4$ | $q_U/4 + 1$ | $q_U/4 + 2$ | |

Table 3: Minimal value of the Taylor expansion parameter q_T for which the scheme is observed to be stable in the numerical experiments considered, given (q_D, q_I) and with $q_U = (2q + 2)$ as in (16) for $q \in \{3, 5\}$.

In this context where no stability result is available then global error estimates cannot be derived for the proposed scheme. Rather, we focus here on the local truncation error that is defined by replacing the numerical solution \mathbf{u}_i^n by the exact continuous solution $\mathbf{u}(x_i, t_n)$ in the numerical scheme.

Definition 1. *Owing to (11-12), the local truncation error $\mathcal{L}(x_i, t_n)$ at the node x_i and time step t_n is defined as*

$$\mathcal{L}(x_i, t_n) = \frac{1}{\Delta t} (\mathbf{u}(x_i, t_{n+1}) - \mathbf{u}(x_i, t_n)) - \frac{1}{\Delta t} \sum_{s=-K/2}^{+K/2} \sum_{m=1}^K \nu_{K,m,s} \left(\frac{\Delta t}{\Delta x} \mathbb{A} \right)^m \mathbf{u}(x_{i+s}, t_n). \quad (41)$$

When a phantom value $\mathbf{u}^(x_{i+s}, t_n)$ is needed at a node x_{i+s} , then it is computed using Approximation 1 based on the the exact continuous solution.*

In this setting, we arrive at the key result of this section where the local truncation error at the irregular points is analyzed in the general case of the ADER- K schemes. These points are chosen as they necessitate a particular treatment which requires to change the local truncation error analysis that could be done in a homogeneous medium or for a regular point.

Property 2. *Let us assume sufficiently smooth initial data, so that the local truncation error for the ADER- K scheme in a homogeneous domain is $\mathcal{O}(\Delta x^K)$. We consider the orders $q = \{3, 5\}$ and we set $q_T = q_U/4$ so that \mathbb{M} in (27) is a square matrix. Then, considering the approximations 1 and 2, the local truncation error in (1) satisfies $\mathcal{L}(x_i, t_n) = \mathcal{O}(\Delta x^\delta)$ with the parameter δ being given by*

$$\delta = \begin{cases} \min(K, q - 1) & \text{for } q = 3, \\ \min(K, q - 1, q_D, q_I - 1) & \text{for } q = 5, \end{cases} \quad (42)$$

at the irregular points $i = I_L - 1, I_L$ on the left of the enlarged interface and

$$\delta = \min(K, q - 1, q_D, q_I - 1) \quad \text{for } q = \{3, 5\}, \quad (43)$$

at the irregular points $i = I_R, I_R + 1$ on the right of the enlarged interface.

Proof. See [Appendix A](#). □

Considering Property 2 and the above discussion on the numerical stability, then one can conclude that a third-order accuracy can be reached but the fourth-order accuracy of the ADER-4 scheme cannot be recovered locally. In the numerical experiments of Section 5.1, global errors are measured and they are found to be in agreement with the analysis of the local error provided in Property 2. Note that, even if Property 2 is relative to the 1D case, the numerical experiments of Section 5.2 suggest that similar results also hold in the 2D case.

In Section 3.5, it has been chosen to express \mathbf{U}_+^q in terms of \mathbf{U}_-^q . The choice is arbitrary and with no consequence when considering the exact continuous solutions. However, in the numerical implementation of this approach, discretization errors in the auxiliary variables \mathbf{Z}^n yields the asymmetry of Property 2 in the local truncation errors associated with the left and right irregular points.

Lastly, in the non-resonant case, no auxiliary variables need to be defined and $\mathbf{Z}(t_n) = \mathbf{0}$ can be set in (18). In this case, the integration and derivation steps of Section 3.6 are irrelevant so that the associated parameters q_I and q_D can be removed from the estimates of Property 2. As a consequence, the error $\mathcal{L}(x_i, t_n) = \mathcal{O}(\Delta x^{\min(K, q-1)})$ for all q is recovered, which meets the result proven in [13] for $K = 2$.

4. Numerical modeling in 2D: an overview

4.1. Setting and implementation

In this section, we formally extend the 2D model (7) to a configuration with a curved enlarged interface defined by two parallel curves $\Gamma_j = \Gamma_j(x_1(s), x_2(s))$, with $j = 0, 1$ and s being the associated curvilinear abscissa, see Figure 3. The solution is defined in the domains on each side, which are denoted as Ω_0 and Ω_1 , while as previously no physical field is defined in the interspace between Γ_0 and Γ_1 of width a . The jump conditions in (7), which are expressed in Cartesian coordinates are directly transposed in the local frame defined by the normal and

tangent vectors $\boldsymbol{\nu}$ and $\boldsymbol{\tau}$ at the interfaces, see Remark 1:

$$\left\{ \begin{array}{ll} \partial_t \mathbf{v}(\mathbf{x}, t) = -\frac{1}{\rho_m} \nabla p(\mathbf{x}, t) & (\mathbf{x} \in \Omega_0 \cup \Omega_1) \\ \partial_t p(\mathbf{x}, t) = -\frac{1}{\chi_m} \operatorname{div} \mathbf{v}(\mathbf{x}, t) & (\mathbf{x} \in \Omega_0 \cup \Omega_1) \\ \partial_t G_r(s, t) = -\omega_r^2 J_r(s, t) + (c_m \alpha_r)^2 \langle \Delta \operatorname{div} \mathbf{v}(\mathbf{x}, t) \rangle_a & (s \in \mathbb{R}, r = 1, \dots, N_R) \\ \partial_t J_r(s, t) = G_r(s, t) & (s \in \mathbb{R}, r = 1, \dots, N_R) \\ \llbracket p \rrbracket_a = B_1 \langle \partial_\nu p \rangle_a + B_2 \langle \partial_\tau p \rangle_a & (s \in \mathbb{R}) \\ \llbracket v_1 \rrbracket_a = C_{11} \langle \partial_\nu v_\nu \rangle_a + C_{12} \langle \partial_\tau v_\nu \rangle_a + C_{22} \langle \partial_\tau v_\tau \rangle_a + h \alpha_0 \langle \operatorname{div} \mathbf{v} \rangle_a - h \sum_{r=1}^{N_R} J_r & (s \in \mathbb{R}) \end{array} \right. \quad (44)$$

where $v_\nu = \mathbf{v} \cdot \boldsymbol{\nu} / \|\boldsymbol{\nu}\|$, $v_\tau = \mathbf{v} \cdot \boldsymbol{\tau} / \|\boldsymbol{\tau}\|$ and $\partial_\nu f = \nabla f \cdot \boldsymbol{\nu} / \|\boldsymbol{\nu}\|$, $\partial_\tau f = \nabla f \cdot \boldsymbol{\tau} / \|\boldsymbol{\tau}\|$. Moreover, $\llbracket f \rrbracket_a$ and $\langle f \rangle_a$ stand for the 2D version of the jump and the mean value of f at the enlarged interface respectively.

Remark 5. *In the proposed extension (44) of the model (7) to a configuration involving a curved enlarged interface, we have chosen to keep the term $\langle \operatorname{div} \mathbf{v} \rangle_a$ as such as it has a clear interpretation relatively to a homogenization process, see (3) and [22]. However, we do not claim that (44) is a homogenized model and our objective is rather to show that such a model can be efficiently handled using the proposed approach.*

As previously, we use the ADER-4 scheme with a uniform Cartesian grid with $\mathbf{u}_{i,j}^n$ denoting the numerical value of the solution $\mathbf{u} = (p, v_1, v_2)^\top$ at the point $(x_i = i\Delta x, x_j = j\Delta x)$ and time t_n . In this framework, the approach adopted is as in 1D: the irregular points are detected and phantom values are computed at the grid points that are located in between Γ_1 and Γ_0 and used by the stencil. For Q being such a point, let Ω^+ and Ω^- denote the closest domain and the farthest one respectively (there is no ambiguity in these definitions as the width of the stencil is systematically chosen to be smaller than the width a of the enlarged interface). Then Q^\pm denotes the orthogonal projection of Q on $\Gamma^\pm = \partial\Omega^\pm$ (see Figure 3).

Extending to the 2D case the definition (15) and (22), a phantom value \mathbf{u}^* at the point Q is defined as a smooth expansion of the value $\mathbf{U}_+^q(t_n)$ of the solution on the Γ^+ interface at the time step t_n . As in (22), this computation relies on a matrix $\mathbb{T}^q(Q, Q^+)$ of the polynomial forms of the 2D Taylor expansion between the points Q and Q^+ . Moreover, the vector $\mathbf{U}_+^q(t_n)$ of size $3(q+1)(q+2)/2$ contains the 2D derivatives of $\mathbf{u}(Q^+, t_n)$ up to the chosen order q .

4.2. Principal features of the implementation

To compute the phantom values, high-order jump conditions relating $\mathbf{U}_+^q(t_n)$ and $\mathbf{U}_-^q(t_n)$ have to be used and these are obtained by differentiating in time the original jump conditions, as it was done in Section 3.4. However, in 2D, high-order derivatives with respect to the curvilinear abscissa s has to be considered as well. This leads to $(q+1)(q+2)$ equations overall. From there, the number of terms in the vectors $\mathbf{U}_\pm^q(t_n)$ can be reduced based on $q(q+1)/2$ compatibility conditions that can be deduced from the condition $\nabla \wedge \mathbf{v} = \mathbf{0}$, which holds outside the support

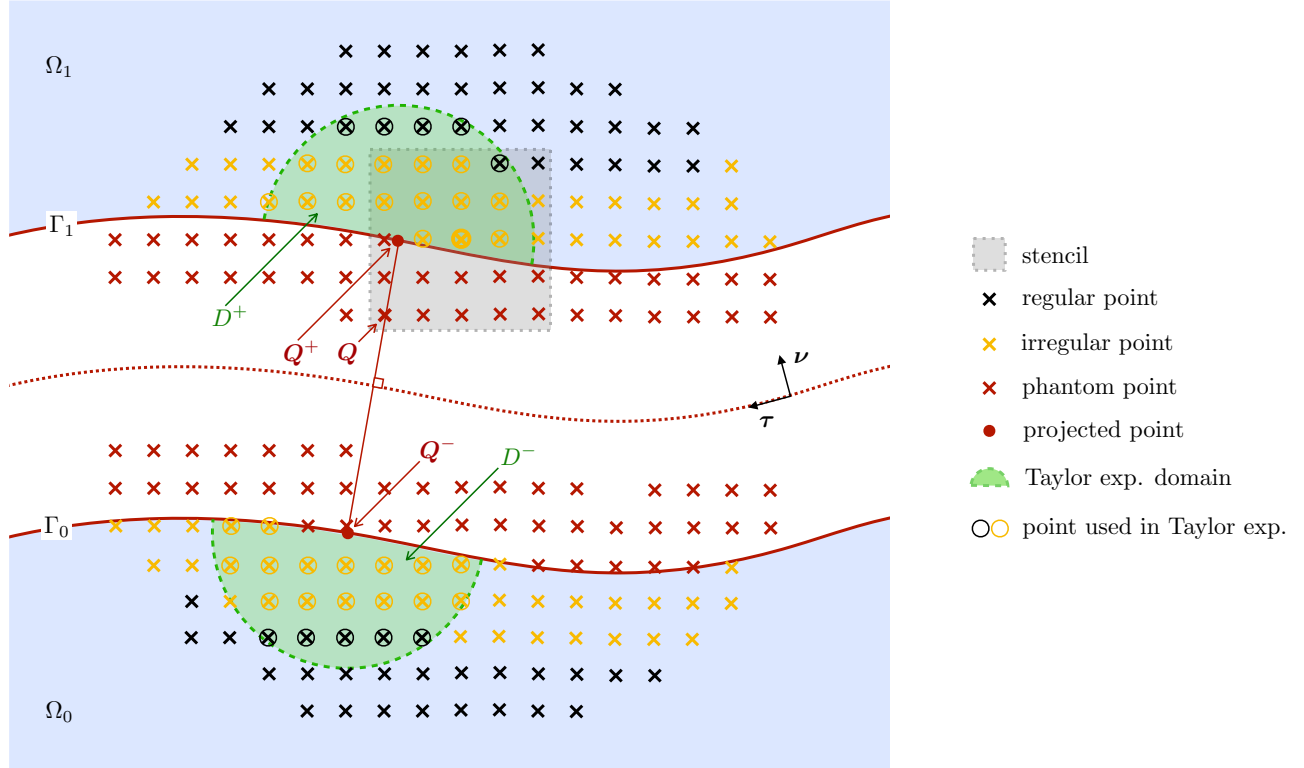


Figure 3: Smooth enlarged interface of width a that separates the domains Ω_0 and Ω_1 in 2D. A phantom value is sought at the point Q whose orthogonal projections onto the interfaces Γ_0 and Γ_1 are denoted as Q^- , Q^+ respectively.

of the external sources considered. The under-determined system of high-order jump conditions so obtained is then solved in the least-squares sense using Singular Value Decomposition.

Next, 2D Taylor expansions are written out at the grid points that are contained in the domain D^+ (resp. D^-) defined as the intersection of the disk centered at Q^+ (resp. Q^-) with the domain Ω^+ (resp. Ω^-), see Figure 3. This allows to compute $\mathbf{U}_+^q(t_n)$ and finally to derive a formula for the numerical approximation $(\mathbf{u}^*)_{i,j}^n$ of the phantom values, as in Approximation 1, by neglecting the Taylor remainders and the derivatives of order $q + 1$. This procedure constitutes an extension of the approach developed in [14] for non-resonant interface problems.

Unlike the non-resonant case, it remains however to compute the numerical approximations J_r^n , G_r^n of the auxiliary variables $J_r(s, t)$ and $G_r(s, t)$ along the enlarged interface. This is achieved by performing numerical integration and numerical differentiation, which extends Approximation 2 in 2D. Note that we limit ourself to $q = 3$ because when $q > 3$ the featured derivatives with respect to the curvilinear abscissa s involve spatial derivatives of the auxiliary variables. Handling the latter in a manner consistent with the proposed approach would in turn require to use additional auxiliary variables. This can be done but we prefer to avoid such technicalities given the satisfying numerical results already obtained for $q = 3$.

| | | | | | | | | | |
|-----------|--------------|---------|-----------------------------------|-------|-------|-----|-----|-----|-----|
| B_1 (m) | C_{11} (m) | h (m) | r | 0 | 1 | 2 | 3 | 4 | 5 |
| 3.2058 | 0.7558 | 2 | ω_r (rad·s ⁻¹) | | 300 | 450 | 600 | 750 | 900 |
| | | | α_r | 0.314 | 0.462 | 0.4 | 0.2 | 0.1 | 0.1 |

Table 4: Interface parameters for the 1D model (9).

| | | | | | | |
|-------------------------------|----------------------------|------------|-----------|---------|----------------|---------|
| ρ_m (g·m ⁻³) | c_m (m·s ⁻¹) | f_s (Hz) | x_s (m) | a (m) | Δx (m) | ζ |
| 1000 | 1500 | 30 | -9 | 6 | 1.5 | 0.95 |

Table 5: Matrix properties and numerical parameters.

5. Numerical experiments

5.1. 1D case

This section aims at validating the numerical method described in Section 3 for the 1D case and assessing the effects of the resonances for the model considered. The chosen constitutive parameters and numerical ones are provided in the Tables 4 and 5 considering a number $N_R = 5$ of resonant frequencies. The time step follows from the CFL condition $\Delta t = \zeta \Delta x / c_m$ taken for $\zeta = 0.95$. The initial conditions are:

$$\mathbf{u}(x, 0) = (-\rho_m, -1/c_m)^\top g(x - x_s), \quad (45)$$

where

$$g(x) = \begin{cases} \sum_{k=0}^3 A_k \sin(2^k x) & \text{if } -\frac{c_m}{f_s} \leq x \leq 0 \\ 0 & \text{otherwise,} \end{cases} \quad (46)$$

with $A_0 = 1$, $A_1 = -21/32$, $A_2 = 63/768$, and $A_3 = -1/512$, which entails that g is of class C^6 . For the chosen values of c_m and Δx in Table 5 then the number of grid nodes is approximately 33 per wavelength at the central frequency f_s . Moreover, the initialization point x_s is chosen so that the support of the initial time conditions (45) does not intersect the enlarged interface. The corresponding initial pressure and its Fourier spectrum are shown in Figure 4. The final simulation time is chosen so that the wave has not hit yet the boundaries of the computational domain.

Figure 5(a) displays the associated acoustic pressure p computed at the final simulation time $t_f = 94.05$ ms, together with a semi-analytical solution p_{ref} , which is derived in Appendix B. The discrepancy between the two solutions is quantified by defining a global relative error at the final simulation time t_f as follows:

$$\epsilon_p(t_f) = \frac{\|p_{\text{ref}}(\cdot, t_f) - p(\cdot, t_f)\|_{L^2(\Omega_{\text{obs}})}}{\|p_{\text{ref}}(\cdot, t_f)\|_{L^2(\Omega_{\text{obs}})}},$$

where $\Omega_{\text{obs}} = [x_{\text{ini}}; x_{\text{end}}] \setminus [-a/2; a/2]$, with x_{ini} and x_{end} the left and right boundaries of the computational domain. One measures $\epsilon_p(t_f) = 1.5 \cdot 10^{-2}$ when $q = 3$, $(q_D, q_I) = (2, 3)$ and $\lambda/\Delta x = 33$ for the characteristic wavelength $\lambda = c_m/f_s$. The relative error $\epsilon_p(t_f)$ is represented as a function of $\lambda/\Delta x$ whose slope in a log-log scale graph characterizes the global order of the scheme, see Figure 5(b) for $q = 3$ and two values of (q_D, q_I) . The errors obtained in the non-resonant case, with $\alpha_r = 0$ for $r = 0, \dots, 5$, are included in Fig. 5(b) for comparison. It is

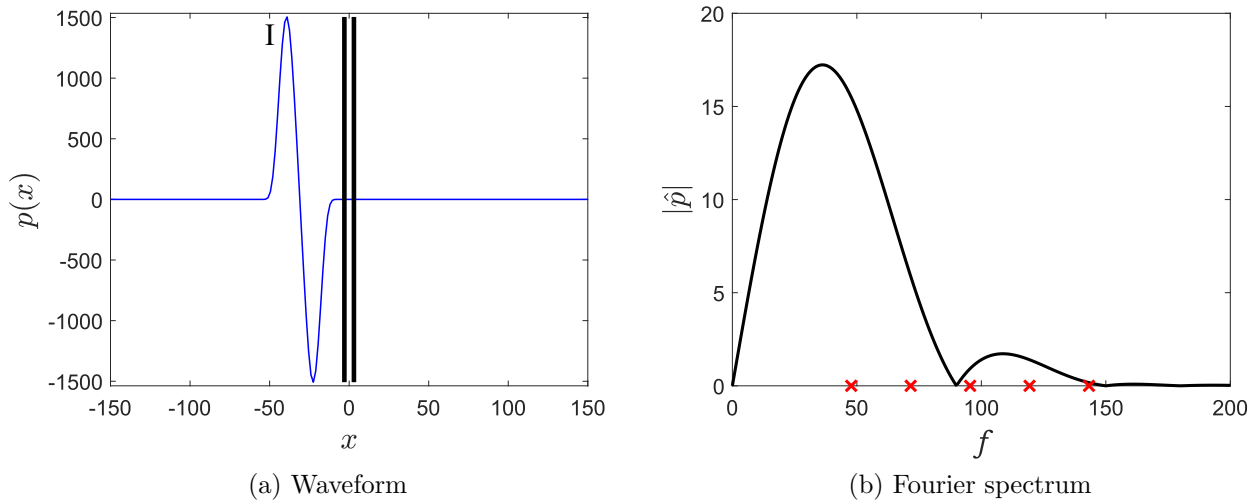


Figure 4: Initial condition (45): (a) pressure field p and (b) associated spectrum with the red crosses indicating the five resonant frequencies $f_r = \omega_r/2\pi$ considered.

seen that setting $(q_D, q_I) = (1, 2)$ yields order 1, which is a drop in accuracy compared to the non-resonant case for which the global error considered is of order 2. The choice $(q_D, q_I) = (2, 3)$ allows to recover this order with comparable accuracy.

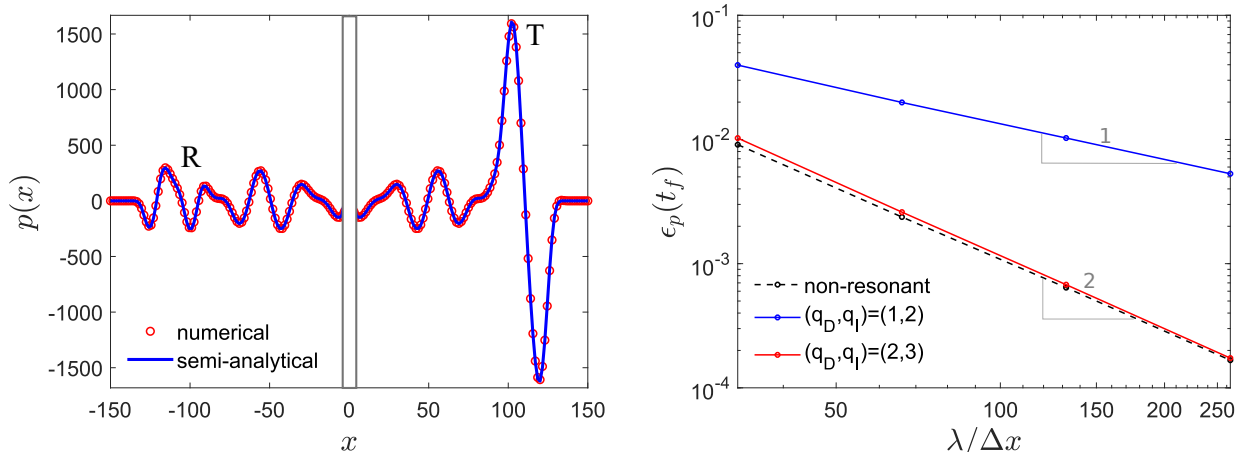
| $q_D \backslash q_I$ | 2 | 3 | 4 | 5 |
|----------------------|---|---|---|---|
| 1 | 1 | 1 | 1 | 1 |
| 2 | 1 | 2 | 2 | 2 |
| 3 | 1 | 2 | 2 | 2 |
| 4 | 1 | 2 | 2 | |

| $q_D \backslash q_I$ | 2 | 3 | 4 | 5 |
|----------------------|---|---|---|---|
| 1 | 1 | 1 | 1 | 1 |
| 2 | 1 | 2 | 2 | 2 |
| 3 | 1 | 2 | 3 | 3 |
| 4 | 1 | 2 | 3 | |

Table 6: Convergence measurements in the 1D case: accuracy orders for $q = 3$ (left) and $q = 5$ (right).

Table 6 reports the orders of accuracy measured using the *global* error metric $\epsilon_p(t_f)$ for $q = 3$ and $q = 5$ depending on the chosen values (q_D, q_I) . The parameter q_T is chosen to be the minimal value given by Table 3 for each value of (q_D, q_I) . These orders, as well as Figure 5(b), are obtained with the relative position of the interfaces within the Cartesian grid being kept while the ratio $\lambda/\Delta x$ is increased. Even if the one lacks of a theoretical stability property for the proposed scheme, these numerical results are in agreement with the analysis of the *local* truncation error in Property 2. Note that, in practice, for the largest values of (q_D, q_I) considered then the Taylor expansion parameter q_T must be increased to maintain the numerical stability. Doing so, the matrix \mathbb{M} is no longer a square matrix so that Property 2 does not apply anymore. However the corresponding orders measured remain compatible with the estimates of Property 2. The right bottom boxes are not filled in Table 6 because, the associated values q_T being too large, the use of the pseudo-inverse of the matrix \mathbb{M} yields unacceptable numerical errors.

After this validation of the one-dimensional method, we can investigate the effects of the resonances. Figure 6 displays the seismograms of the pressure field with resonances in the jump



(a) p_{ref} (blue) and p (red) at the final simulation time $t_f = 94.05$ ms. R: reflected wave, T: transmitted wave.

(b) Relative error $\epsilon_p(t_f)$ in a log-log scale.

Figure 5: Numerical results for pressure field p in the 1D case: comparison with a semi-analytical solution p_{ref} .

conditions and without (i.e. when $\alpha_r = 0$ for $r = 0, \dots, 5$). This figure highlights the resonant behavior of the wavefield, with energy being radiated away from the enlarged interface long after the passing of the incident wave. This is a consequence of the frequency dependence of the parameter $\mathcal{D}(\omega)$ in (5) that intervenes in the definition of the jump conditions of the model (3) considered.

5.2. 2D case

In this section, we validate the method discussed in Section 4 on three test cases: i) incident plane wave at normal incidence on a plane enlarged interface, ii) slanted incident plane wave on a tilted enlarged interface, and iii) incident plane wave on a circular enlarged interface. Semi-analytical solutions are computed in these three cases, see Appendix B and Appendix C. The initial conditions are

$$\mathbf{u}(\mathbf{x}, 0) = (p, v_1, v_2)^\top(\mathbf{x}, 0) = -(\rho_m, \cos \theta_I / c_m, \sin \theta_I / c_m)^\top g((x_1 - x_{s1}) \cos \theta_I + (x_2 - x_{s2}) \sin \theta_I), \quad (47)$$

where g is defined in (46), θ_I is the angle between the direction of propagation of the plane wave and the horizontal axis and the initialization point $\mathbf{x}_s = (x_{s1}, x_{s2})$ is chosen so that the support of the initial time conditions does not intersect the enlarged interface. The constitutive and numerical parameters are those of the tables 4 and 5 while the chosen additional interface parameters that are requested in 2D are reported in Table 7. The proposed numerical method is implemented taking $q = 3$ since, as previously discussed, the cases $q \geq 4$ are very demanding in 2D and require to handle additional auxiliary variables.

| B_2 (m) | C_{12} (m) | C_{22} (m) |
|-----------|--------------|--------------|
| 0.284 | 0.284 | 0.4 |

Table 7: Additional interface parameters for the 2D model (44).

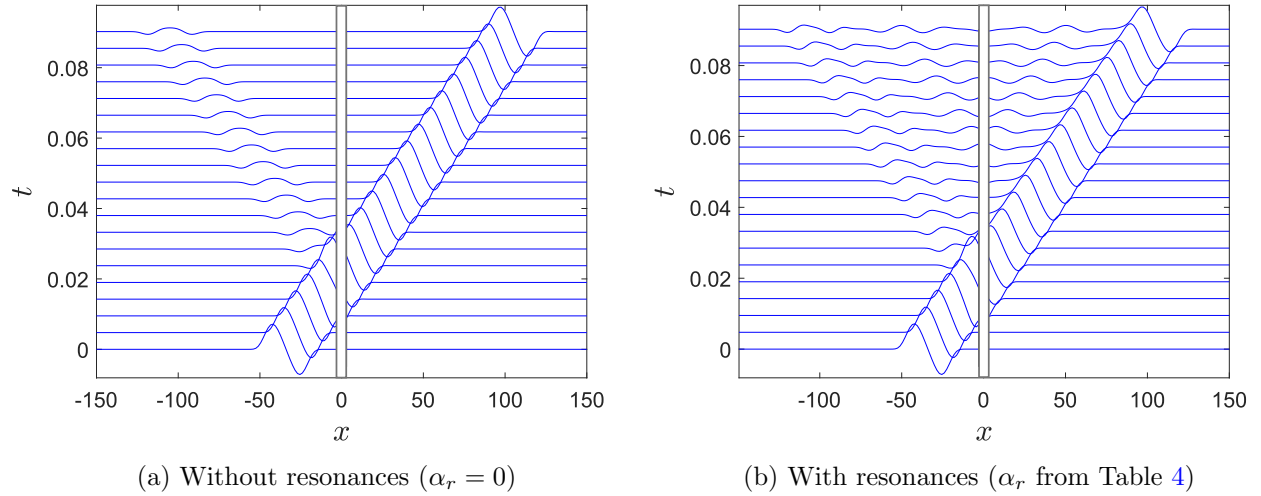


Figure 6: Seismogram of the acoustic pressure p field.

5.2.1. Incident plane wave at normal incidence

First, we consider the case of normal incidence, i.e. $\theta_I = 0$, with a wave impacting normally a plane enlarged interface, in which case the fields are independent of x_2 . Periodicity conditions are imposed at the bottom and top boundaries of the computational domain. Physically, the problem is 1D, but the full 2D algorithm is employed and one sets $(q_D, q_I) = (2, 3)$.

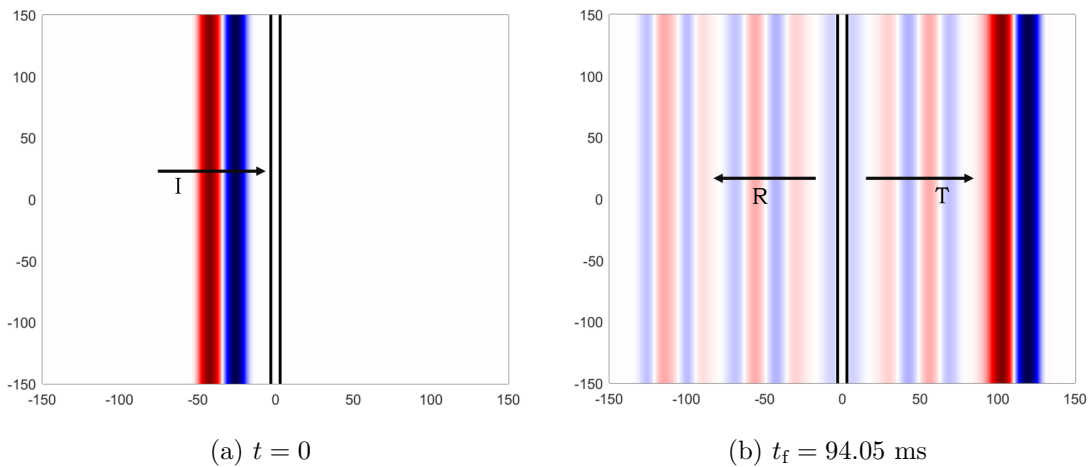


Figure 7: Pressure field p computed for an incident plane wave (I) at normal incidence on the enlarged interface. R: reflected wave, T: transmitted wave.

Figure 7 displays the pressure field p at the initial time $t = 0$, at which the initialization point in (47) is $\mathbf{x}_s = (-9 \text{ m}, 0 \text{ m})$, and at time $t_f = 94.05$ ms, while Figure 8 shows the profiles of the solution at $x_2 = 0$. The discrepancy between the numerical and the semi-analytical solutions is comparable with the 1D results with $\epsilon_p(t_f) = 4.5 \cdot 10^{-2}$ for $\lambda/\Delta x = 33$. Table 8 reports the measured orders of convergence, which are the same than in 1D.

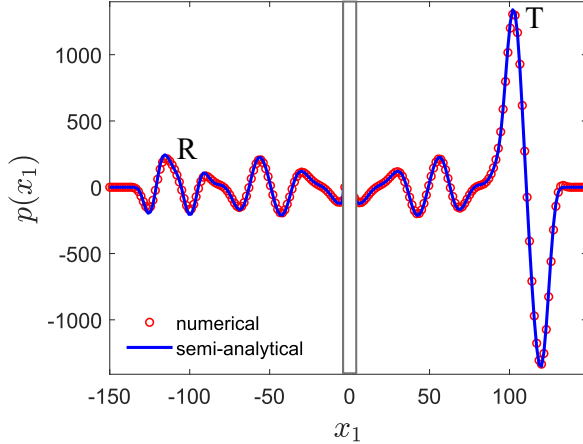


Figure 8: Incident plane wave at normal incidence in 2D: semi-analytical and numerical pressure fields p_{ref} (blue) and p (red) at $x_2 = 0$ and for the final simulation time $t_f = 94.05$ ms.

| $q_D \backslash q_I$ | 2 | 3 | 4 | 5 |
|----------------------|---|---|---|---|
| 1 | 1 | 1 | 1 | 1 |
| 2 | 1 | 2 | 2 | 2 |
| 3 | 1 | 2 | 2 | 2 |
| 4 | 1 | 2 | 2 | |

Table 8: Convergence measurements in the 2D case: accuracy orders for $q = 3$.

5.2.2. Slanted incident plane wave on a tilted enlarged interface

The case of an incident wave at oblique incidence, with $\theta_I = 10^\circ$ in (47), on an enlarged interface tilted from the vertical axis at -7.2° is now considered. It allows us to inspect both the dependencies of the jump conditions on x_2 and the capability of the numerical method to account for the slope of the interfaces on a Cartesian grid. To perform the simulations, one imposes the semi-analytical solution of the problem on the domain boundary.

Figure 9 displays the pressure field computed at the initial time, at which the initialization point in (47) is $\mathbf{x}_s = (-21 \text{ m}, -150 \text{ m})$, and at time $t_f = 84.55$ ms when $(q_D, q_I) = (2, 3)$. Figure 10 compares the reference semi-analytical solution and the numerical one, with $\epsilon_p(t_f) = 4.1 \cdot 10^{-2}$ when $\lambda/\Delta x = 33$. This result is comparable to that given in Section 5.2.1, which illustrates that the dependency of the jump conditions on x_2 and the slope of the interfaces are both accurately accounted for by the proposed numerical method.

5.2.3. Incident plane wave on a circular enlarged interface

The case of an incident plane wave on a circular enlarged interface is now considered. This example allows to inspect the capability of the method to take into account a curved enlarged interface. A semi-analytical solution is derived in Appendix C in the case $B_2 = C_{12} = \alpha_0 = 0$. Consequently, in this subsection, these interface parameters are set to zero to allow the comparison with the semi-analytical solution. The numerical parameters are $(q_D, q_I) = (2, 3)$.

We consider an incident plane wave with propagation direction along x_1 and periodicity conditions imposed on the top and bottom boundaries of the computational domain. The

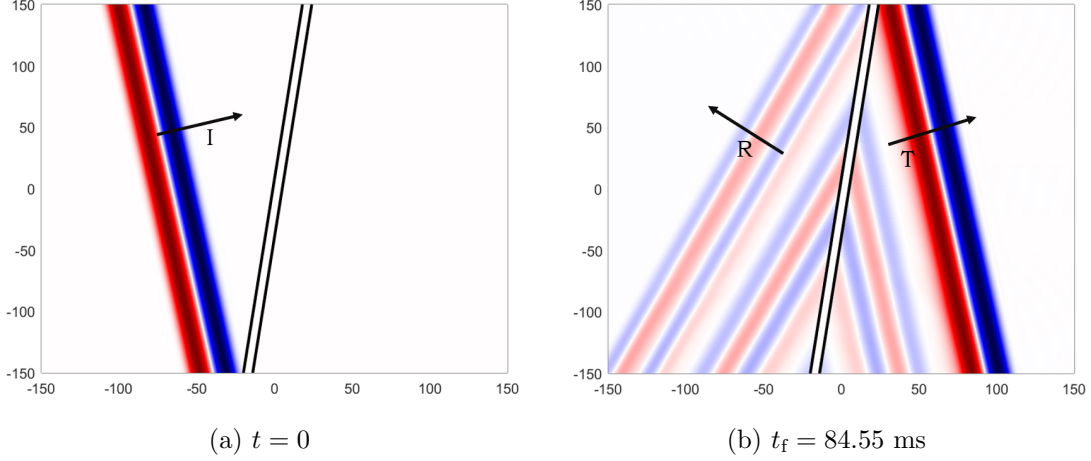


Figure 9: Pressure field p computed for an incident plane wave (I) at oblique incidence on a tilted enlarged interface. R: reflected wave, T: transmitted wave.

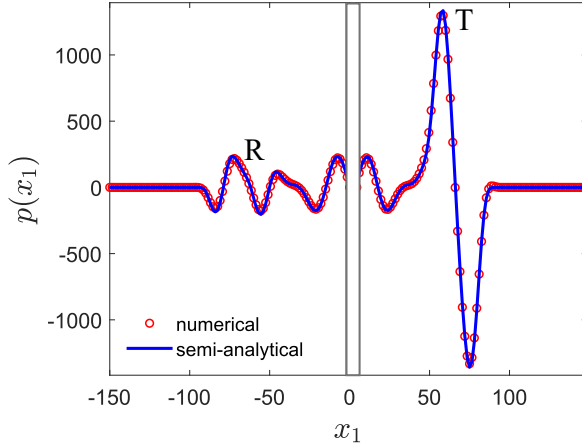


Figure 10: Slanted incident plane wave on a tilted enlarged interface: semi-analytical and numerical pressure fields p_{ref} (blue) and p (red) at $x_2 = 0$ and for the final simulation time $t_f = 84.55$ ms.

pressure field at the initial time, at which the initialization point in (47) is $\mathbf{x}_s = (-45 \text{ m}, 0 \text{ m})$, and at final simulation time $t_f = 63.3$ ms are displayed in Figure 11. The comparison with the semi-analytical solution is reported in Figure 12 at $x_2 = 0$. The measured error is $\epsilon_p(t_f) = 2 \cdot 10^{-2}$ when $\lambda/\Delta x = 33$, which highlights the satisfying performances of the proposed approach with the circular enlarged interface being accurately handled numerically.

6. Conclusion

In this study, our objective was to handle enlarged interfaces characterized by frequency-dependent jump conditions and consequently jump conditions that are non-local in time when formulated in the time domain. A time-domain numerical method was proposed and implemented for this type of model. To the best of our knowledge, this constitutes the first effort to simulate transient wave propagation across such resonant meta-interfaces. The proposed approach relies on the following key points: (i) A set of auxiliary variables is introduced locally

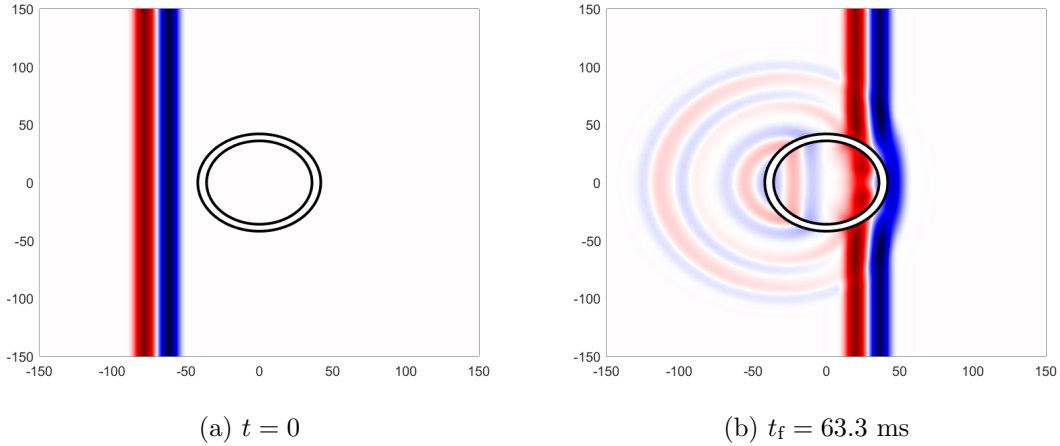


Figure 11: Pressure field p computed for an incident plane wave on a circular enlarged interface.

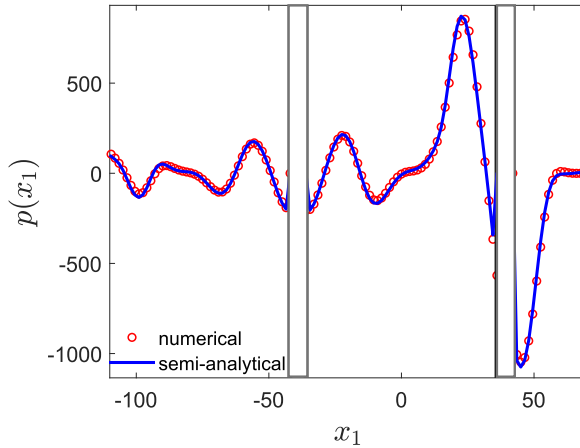


Figure 12: Incident plane wave on a circular enlarged interface in 2D: semi-analytical and numerical pressure fields p_{ref} (blue) and p (red) at $x_2 = 0$ and for the final simulation time $t_f = 63.3$ ms. The vertical black lines denote the position of the enlarged circular interface.

along the enlarged interface, which allows to formulate a first-order system in time with jump conditions that are local in time. (ii) An immersed interface method is developed to handle numerically such a system by using a high-order finite differences scheme on a Cartesian grid while offering a subcell resolution through a proper discretization of the enlarged interface. Local error estimates were derived to assess the optimal values of the featured numerical parameters. The proposed numerical method was then illustrated and validated considering 1D and 2D configurations involving plane waves illuminating straight or curved enlarged interfaces. Moreover, the solutions to these problems were derived and used for quantitative comparisons.

Future directions of work concern the validation of the time-domain interface model considered itself. Indeed, as it has been discussed in the introduction, such resonant meta-interface models can be constructed systematically from the homogenization of a microstructured layer containing inclusions whose constitutive properties have a particular scaling with respect to these of the background medium. With the proposed numerical method at hand then the validity of such effective meta-interface models can be assessed through comparison with full-field

simulations. Another perspective concerns the design of meta-interfaces through the optimization of an underlying microstructured medium to reach some objective effective properties. This is of particular interest in view of, e.g., noise reduction by thin resonant metasurfaces [18, 24]. A promising strategy relies on the topological optimization tools developed in [9, 3].

Appendix A. Proof of Property 2

To prove Property 2, one first estimates the order of the approximation of the phantom values on the left and right sides of the enlarged interface. In the sequel, $\tilde{\mathbf{u}}^*(x_i, t_n)$ denotes the phantom value obtained when replacing the numerical values \mathbf{u}_j^n by the exact continuous solution $\mathbf{u}(x_j, t_n)$ in Approximation 1. This solution is assumed to be as smooth as necessary.

Appendix A.1. Left-side approximation of the phantom value

From the definition (25), we introduce the following vector that features both exact and approximate quantities

$$\mathbf{V}(t_n) = \begin{pmatrix} \mathbf{u}(x_{I_L - q_T + 1}, t_n) \\ \vdots \\ \mathbf{u}(x_{I_L}, t_n) \\ \mathbf{u}(x_{I_R}, t_n) - \mathbb{T}_{I_R}^q(\frac{a}{2})(\mathbb{C}_+^q)^{-1} \mathbb{Q}^q \mathbf{Z}^n \\ \vdots \\ \mathbf{u}(x_{I_R + q_T - 1}, t_n) - \mathbb{T}_{I_R + q_T - 1}^q(\frac{a}{2})(\mathbb{C}_+^q)^{-1} \mathbb{Q}^q \mathbf{Z}^n \end{pmatrix}. \quad (\text{A.1})$$

Using (31), one gets at the left side of the enlarged interface:

$$\tilde{\mathbf{u}}^*(x_i, t_n) = \mathbb{T}_i^q \left(-\frac{a}{2} \right) \mathbb{M}^{-1} \mathbf{V}(t_n). \quad (\text{A.2})$$

Based on (39), one also introduces the $2N_R$ element vector \mathbf{H} that is such that

$$\mathbf{Z}(t_n) = \mathbf{Z}^n + \mathbf{H} \quad (\text{A.3})$$

and whose entries satisfy $\mathbf{H}[i] = \mathcal{O}(\Delta t^{q_D + 2}) + \mathcal{O}(\Delta t^{q_I})$ for $i \in \{1, \dots, N_R\}$ and $\mathbf{H}[i] = \mathcal{O}(\Delta t^{q_D + 1}) + \mathcal{O}(\Delta t^{q_I})$ for $i \in \{N_R + 1, \dots, 2N_R\}$. Then, $\mathbf{V}(t_n)$ can be expressed as:

$$\mathbf{V}(t_n) = \mathbf{U}(t_n) + \mathbf{F}, \quad (\text{A.4})$$

with

$$\mathbf{F} = \begin{pmatrix} \mathbf{0} \\ \vdots \\ \mathbf{0} \\ \mathbb{T}_{I_R}^q(\frac{a}{2})(\mathbb{C}_+^q)^{-1} \mathbb{Q}^q \mathbf{H} \\ \vdots \\ \mathbb{T}_{I_R + q_T - 1}^q(\frac{a}{2})(\mathbb{C}_+^q)^{-1} \mathbb{Q}^q \mathbf{H} \end{pmatrix}, \quad (\text{A.5})$$

so that

$$\tilde{\mathbf{u}}^*(x_i, t_n) = \mathbb{T}_i^q \left(-\frac{a}{2} \right) \mathbb{M}^{-1} \mathbf{U}(t_n) + \mathbb{T}_i^q \left(-\frac{a}{2} \right) \mathbb{M}^{-1} \mathbf{F}. \quad (\text{A.6})$$

Equation (28) is then used to get:

$$\tilde{\mathbf{u}}^*(x_i, t_n) = \mathbb{T}_i^q \left(-\frac{a}{2}\right) \mathbf{U}_-^q(t_n) + \mathbb{T}_i^q \left(-\frac{a}{2}\right) \mathbb{M}^{-1} [\mathbf{\Delta}(t_n) + \mathcal{O}(\Delta x^{q+1}) + \mathbf{F}]. \quad (\text{A.7})$$

Symbolic computations are then performed using Maple to estimate the leading contributions of the entries of the vectors in (A.7). Doing so provides:

$$\left\{ \begin{array}{ll} \mathbb{T}_i^q \left(-\frac{a}{2}\right) \mathbb{M}^{-1} \mathbf{\Delta}(t_n) = \mathcal{O}(\Delta x^q) & \text{for } q = 3 \text{ or } 5, \\ \mathbb{T}_i^q \left(-\frac{a}{2}\right) \mathbb{M}^{-1} \mathcal{O}(\Delta x^{q+1}) = \mathcal{O}(\Delta x^{q+1}) & \text{for } q = 3 \text{ or } 5, \\ \mathbb{T}_i^q \left(-\frac{a}{2}\right) \mathbb{M}^{-1} \mathbf{F} = \begin{pmatrix} \mathcal{O}(\Delta x^{q_D+3}) + \mathcal{O}(\Delta x^{q_I+2}) \\ \mathcal{O}(\Delta x^{q_D+3}) + \mathcal{O}(\Delta x^{q_I+1}) \end{pmatrix} & \text{for } q = 3, \\ \mathbb{T}_i^q \left(-\frac{a}{2}\right) \mathbb{M}^{-1} \mathbf{F} = \begin{pmatrix} \mathcal{O}(\Delta x^{q_D+1}) + \mathcal{O}(\Delta x^{q_I}) \\ \mathcal{O}(\Delta x^{q_D+2}) + \mathcal{O}(\Delta x^{q_I}) \end{pmatrix} & \text{for } q = 5. \end{array} \right. \quad (\text{A.8})$$

Since $q_I \geq 2$ and $q_D \geq 1$, then the entries of the vector $\mathbb{T}_i^q(-\frac{a}{2})\mathbb{M}^{-1}\mathbf{F}$ have a contribution of at most $\mathcal{O}(\Delta x^q)$ when $q = 3$. We eventually get:

$$\tilde{\mathbf{u}}^*(x_i, t_n) = \begin{cases} \mathbb{T}_i^q \left(-\frac{a}{2}\right) \mathbf{U}_-^q(t_n) + \mathcal{O}(\Delta x^q) & \text{for } q = 3, \\ \mathbb{T}_i^q \left(-\frac{a}{2}\right) \mathbf{U}_-^q(t_n) + \mathcal{O}(\Delta x^{\min(q, q_D+1, q_I)}) & \text{for } q = 5. \end{cases} \quad (\text{A.9})$$

Appendix A.2. Right-side approximation of the phantom value

Owing to (31), one considers the following identity at the right-side of the enlarged interface:

$$\tilde{\mathbf{u}}^*(x_i, t_n) = \mathbb{T}_i^q \left(\frac{a}{2}\right) (\mathbb{C}_+^q)^{-1} [\mathbb{C}_-^q \mathbb{M}^{-1} \mathbf{V}(t_n) + \mathbb{Q}^q \mathbf{Z}^n]. \quad (\text{A.10})$$

Using (A.3) and (A.4), the previous equation can be recast as:

$$\tilde{\mathbf{u}}^*(x_i, t_n) = \mathbb{T}_i^q \left(\frac{a}{2}\right) (\mathbb{C}_+^q)^{-1} [\mathbb{C}_-^q \mathbb{M}^{-1} \mathbf{U}(t_n) + \mathbb{Q}^q \mathbf{Z}(t_n) + \mathbb{C}_-^q \mathbb{M}^{-1} \mathbf{F} - \mathbb{Q}^q \mathbf{H}]. \quad (\text{A.11})$$

Moreover, combining (28) and (26) one gets

$$\mathbb{C}_-^q \mathbb{M}^{-1} \mathbf{U}(t_n) = \mathbb{C}_-^q \mathbf{U}_-^q(t_n) + (\mathbf{R}_-^q(t_n) - \mathbf{R}_+^q(t_n)) + \mathbb{G}(\mathbf{R}_-^q(t_n) - \mathbf{R}_+^q(t_n)) + \mathbb{C}_-^q \mathbb{M}^{-1} \mathcal{O}(\Delta x^{q+1}), \quad (\text{A.12})$$

where the matrix \mathbb{G} is defined as

$$\mathbb{G} = \mathbb{C}_-^q \mathbb{M}^{-1} \begin{pmatrix} \mathbf{0} \\ \vdots \\ \mathbf{0} \\ \mathbb{T}_{I_R}^q \left(\frac{a}{2}\right) (\mathbb{C}_+^q)^{-1} \\ \vdots \\ \mathbb{T}_{I_{R+q_T-1}}^q \left(\frac{a}{2}\right) (\mathbb{C}_+^q)^{-1} \end{pmatrix} - \mathbb{I}_{2q} \quad (\text{A.13})$$

in terms of the identity matrix \mathbb{I}_{2q} of order $2q$. Inserting (A.12) in (A.11) and using (18) then entails:

$$\begin{aligned} \tilde{\mathbf{u}}^*(x_i, t_n) = \mathbb{T}_i^q \left(\frac{a}{2} \right) \mathbf{U}_+^q(t_n) + \mathbb{T}_i^q \left(\frac{a}{2} \right) (\mathbb{C}_+^q)^{-1} [\mathbb{G}(\mathbf{R}_-^q(t_n) - \mathbf{R}_+^q(t_n)) \\ + \mathbb{C}_-^q \mathbb{M}^{-1} \mathcal{O}(\Delta x^{q+1}) + \mathbb{C}_-^q \mathbb{M}^{-1} \mathbf{F} - \mathbb{Q}^q \mathbf{H}]. \end{aligned} \quad (\text{A.14})$$

Symbolic computations using Maple lead to the following estimates for $q = 3$ or 5 :

$$\begin{cases} \mathbb{T}_i^q \left(\frac{a}{2} \right) (\mathbb{C}_+^q)^{-1} \mathbb{G}(\mathbf{R}_-^q(t_n) - \mathbf{R}_+^q(t_n)) = \mathcal{O}(\Delta x^q), \\ \mathbb{T}_i^q \left(\frac{a}{2} \right) (\mathbb{C}_+^q)^{-1} \mathbb{C}_-^q \mathbb{M}^{-1} \mathcal{O}(\Delta x^{q+1}) = \mathcal{O}(\Delta x^{q+1}), \\ \mathbb{T}_i^q \left(\frac{a}{2} \right) (\mathbb{C}_+^q)^{-1} \mathbb{C}_-^q \mathbb{M}^{-1} \mathbf{F} = \begin{pmatrix} \mathcal{O}(\Delta x^{qD+1}) + \mathcal{O}(\Delta x^{qI}) \\ \mathcal{O}(\Delta x^{qD+2}) + \mathcal{O}(\Delta x^{qI}) \end{pmatrix}. \end{cases} \quad (\text{A.15})$$

Note that the first of the above estimates makes use of the definition (21) of $\mathbf{R}_\pm^q(t_n)$, which are expressed in terms of the exact solution and assumes that the latter is sufficiently smooth. From the definition of \mathbf{H} in (A.3) and owing to Property 1, it follows also that

$$\mathbb{T}_i^q \left(\frac{a}{2} \right) (\mathbb{C}_+^q)^{-1} \mathbb{Q}^q \mathbf{H} = \begin{pmatrix} \mathcal{O}(\Delta x^{qD+1}) + \mathcal{O}(\Delta x^{qI}) \\ \mathcal{O}(\Delta x^{qD+2}) + \mathcal{O}(\Delta x^{qI}) \end{pmatrix}. \quad (\text{A.16})$$

Therefore, for $q = 3$ or 5 , we finally obtain the following estimate for the right-side approximation of the phantom values

$$\tilde{\mathbf{u}}^*(x_i, t_n) = \mathbb{T}_i^q \left(\frac{a}{2} \right) \mathbf{U}_+^q(t_n) + \mathcal{O}(\Delta x^{\min(q, qD+1, qI)}). \quad (\text{A.17})$$

Appendix A.3. Local truncation error

With the left-side and right-side approximations (A.9) and (A.17) at hand, we now turn to the estimation of the local truncation error. To do so, one considers the irregular point x_{I_R} since it is on the right side of the enlarged interface that the approximation of the phantom value is expected to be the less accurate. Note that the result to come applies for any irregular point at the right-side and its proof would follow the same steps for left-side points. According to the ESIM, the time-stepping (12) at the irregular point x_{I_R} is recast as

$$\begin{aligned} \frac{\mathbf{u}_{I_R}^{n+1} - \mathbf{u}_{I_R}^n}{\Delta t} + \frac{1}{\Delta t} \sum_{s=-K/2}^{-1} \sum_{m=1}^K \nu_{K,m,s} \left(\mathbb{A} \frac{\Delta t}{\Delta x} \right)^m \mathbf{u}_{I_R+s}^{*n} \\ + \frac{1}{\Delta t} \sum_{s=0}^{K/2} \sum_{m=1}^K \nu_{K,m,s} \left(\mathbb{A} \frac{\Delta t}{\Delta x} \right)^m \mathbf{u}_{I_R+s}^n = \mathbf{0}. \end{aligned} \quad (\text{A.18})$$

Remark 6. *In this article, the computation of the phantom values has been discussed for the ADER-4 scheme for the sake of simplicity. Yet, the only difference between the different ADER-K schemes is the number of irregular points and phantom points to be considered. Therefore, the local truncation error at x_{I_R} , which is always an irregular point, is here analyzed for a ADER-K scheme, with K being an arbitrary even integer.*

To estimate the local truncation error $\mathcal{L}(x_{I_R}, t_n)$ of Definition 1, each numerical value \mathbf{u}_i^n in (A.18) is replaced by the exact continuous value $\mathbf{u}(x_i, t_n)$ and each phantom value \mathbf{u}_i^{*n} is replaced by $\tilde{\mathbf{u}}^*(x_i, t_n)$. Then, we use standard Taylor expansions and (A.17) for each of these terms respectively as

$$\begin{cases} \mathbf{u}(x_{I_R+s}, t_n) = \sum_{\ell=0}^q \frac{1}{\ell!} \left(x_{I_R+s} - \frac{a}{2}\right)^\ell \partial_x^\ell \mathbf{u} \left(\frac{a}{2}, t_n\right) + \mathcal{O}(\Delta x^{q+1}), \\ \tilde{\mathbf{u}}^*(x_{I_R+s}, t_n) = \sum_{\ell=0}^q \frac{1}{\ell!} \left(x_{I_R+s} - \frac{a}{2}\right)^\ell \partial_x^\ell \mathbf{u} \left(\frac{a}{2}, t_n\right) + \mathcal{O}(\Delta x^{\min(q, q_D+1, q_I)}). \end{cases} \quad (\text{A.19})$$

Since $\Delta t = \mathcal{O}(\Delta x)$ holds from the CFL condition, then one can write

$$\mathcal{L}(x_{I_R}, t_n) = \mathcal{L}_0(x_{I_R}, t_n) + \sum_{m=1}^K \mathcal{L}_m(x_{I_R}, t_n) + \mathcal{O}(\Delta x^{\min(q-1, q_D, q_I-1)}), \quad (\text{A.20})$$

when, for $m = 1, \dots, K$, defining:

$$\begin{aligned} \mathcal{L}_0(x_{I_R}, t_n) &= \frac{1}{\Delta t} (\mathbf{u}(x_{I_R}, t_{n+1}) - \mathbf{u}(x_{I_R}, t_n)), \\ \mathcal{L}_m(x_{I_R}, t_n) &= \frac{1}{\Delta t} \sum_{s=-K/2}^{+K/2} \nu_{K,m,s} \left(\mathbb{A} \frac{\Delta t}{\Delta x}\right)^m \sum_{\ell=0}^q \frac{1}{\ell!} \left(x_{I_R+s} - \frac{a}{2}\right)^\ell \partial_x^\ell \mathbf{u} \left(\frac{a}{2}, t_n\right). \end{aligned} \quad (\text{A.21})$$

From a Taylor expansion at the order K in time and using (11) in combination with Taylor expansions at the order $q - m$ in space, we can write

$$\begin{aligned} \mathbf{u}(x_{I_R}, t_{n+1}) &= \mathbf{u}(x_{I_R}, t_n) + \sum_{m=1}^K \frac{\Delta t^m}{m!} (-1)^m \mathbb{A}^m \sum_{\ell=0}^{q-m} \frac{1}{\ell!} \left(x_{I_R} - \frac{a}{2}\right)^\ell \partial_x^{m+\ell} \mathbf{u} \left(\frac{a}{2}, t_n\right) \\ &\quad + \mathcal{O}(\Delta x^{q+1}) + \mathcal{O}(\Delta x^{K+1}). \end{aligned} \quad (\text{A.22})$$

Combining (A.21) and (A.22), we can rewrite $\mathcal{L}_0(x_{I_R}, t_n)$ as follows:

$$\begin{aligned} \mathcal{L}_0(x_{I_R}, t_n) &= \frac{1}{\Delta t} \sum_{m=1}^K \frac{\Delta t^m}{m!} (-1)^m \mathbb{A}^m \sum_{\ell=m}^q \frac{1}{(\ell-m)!} \left(x_{I_R} - \frac{a}{2}\right)^{\ell-m} \partial_x^\ell \mathbf{u} \left(\frac{a}{2}, t_n\right) \\ &\quad + \mathcal{O}(\Delta x^q) + \mathcal{O}(\Delta x^K). \end{aligned} \quad (\text{A.23})$$

Summing \mathcal{L}_0 and the \mathcal{L}_m yields:

$$\mathcal{L}(x_{I_R}, t_n) = \frac{1}{\Delta t} \sum_{m=1}^K \mathbb{A}^m \Delta t^m \sum_{\ell=0}^q \varepsilon_{\ell,m} \partial_x^\ell \mathbf{u} \left(\frac{a}{2}, t_n\right) + \mathcal{O}(\Delta x^{\min(K, q-1, q_D, q_I-1)}), \quad (\text{A.24})$$

where, for $m = 1, \dots, K$ and $\ell = 0, \dots, q$, the parameter $\varepsilon_{\ell,m}$ is defined as

$$\varepsilon_{\ell,m} = \frac{(-1)^m}{m!(\ell-m)!} \left(x_{I_R} - \frac{a}{2}\right)^{\ell-m} \delta_{\ell \geq m} + \sum_{s=-K/2}^{K/2} \nu_{K,m,s} \frac{1}{\ell! \Delta x^m} \left(x_{I_R} - \frac{a}{2} + s\Delta x\right)^\ell, \quad (\text{A.25})$$

with $\delta_{\ell \geq m} = 0$ if $\ell < m$ and $\delta_{\ell \geq m} = 1$ else. Expanding the second right-hand side term using the binomial expansion entails

$$\varepsilon_{\ell, m} = \frac{(-1)^m}{m!(\ell - m)!} \left(x_{I_R} - \frac{a}{2}\right)^{\ell - m} \delta_{\ell \geq m} + \sum_{j=0}^{\ell} \frac{\Delta x^{j-m}}{j!(\ell - j)!} \left(x_{I_R} - \frac{a}{2}\right)^{\ell - j} \sum_{s=-K/2}^{K/2} \nu_{K, m, s} s^j. \quad (\text{A.26})$$

For $0 \leq j \leq K$ then (14) implies that it holds:

$$\frac{(-1)^m}{m!(\ell - m)!} \left(x_{I_R} - \frac{a}{2}\right)^{\ell - m} \delta_{\ell \geq m} + \sum_{j=0}^{\min(\ell, K)} \frac{\Delta x^{j-m}}{j!(\ell - j)!} \left(x_{I_R} - \frac{a}{2}\right)^{\ell - j} \sum_{s=-K/2}^{K/2} \nu_{K, m, s} s^j = 0. \quad (\text{A.27})$$

Therefore, if $\ell \leq K$ then $\varepsilon_{\ell, m} = 0$ and when $\ell > K$ then (A.25) reduces to

$$\varepsilon_{\ell, m} = \sum_{j=K+1}^{\ell} \frac{\Delta x^{j-m}}{j!(\ell - j)!} \left(x_{I_R} - \frac{a}{2}\right)^{\ell - j} \sum_{s=-K/2}^{K/2} \nu_{K, m, s} s^j = \mathcal{O}(\Delta x^{\ell - m}) \sum_{j=K+1}^{\ell} \sum_{s=-K/2}^{K/2} \frac{\nu_{K, m, s} s^j}{j!(\ell - j)!}.$$

The results for these two cases can be summarized as follows for all (ℓ, m) :

$$\varepsilon_{\ell, m} = \mathcal{O}(\Delta x^{\ell - m}) \delta_{\ell > K}. \quad (\text{A.28})$$

This allows to conclude the proof of Proposition 2 since, using (A.28) in (A.24), then for $q = 3$ and $q = 5$ one gets:

$$\mathcal{L}(x_{I_R}, t_n) = \mathcal{O}(\Delta x^{\min(K, q-1, q_D, q_I-1)}). \quad (\text{A.29})$$

Appendix B. Semi-analytical solution for a plane wave on a plane interface

We consider an incident plane wave at an angle θ_I with the horizontal axis and an enlarged interface located between the *physical* points $x_1 = x_l$ and $x_1 = x_r$, see Figure B.13. The initial conditions are given in (47). To calculate the solution to the 2D problem (44) in this configuration, we consider its frequency-domain formulation (3). The wavefield solution $\hat{\mathbf{u}}(\mathbf{x}, \omega)$ is then decomposed into incident $\hat{\mathbf{u}}_I$, reflected $\hat{\mathbf{u}}_R$ and transmitted $\hat{\mathbf{u}}_T$ waves, ie $\hat{\mathbf{u}} = \hat{\mathbf{u}}_I + \hat{\mathbf{u}}_R + \hat{\mathbf{u}}_T$. It is assumed that these are plane waves that write

$$\begin{cases} \hat{\mathbf{u}}_I = \begin{pmatrix} -\rho_m \\ -\cos \theta_I / c_m \\ -\sin \theta_I / c_m \end{pmatrix} \exp(-\mathbf{k}_I \cdot (\mathbf{x} - \mathbf{x}_s)) \hat{g}(\omega), \\ \hat{\mathbf{u}}_R = \begin{pmatrix} -\rho_m \\ -\cos \theta_R / c_m \\ -\sin \theta_R / c_m \end{pmatrix} \exp(-\mathbf{k}_R \cdot (\mathbf{x} - \mathbf{x}_s)) \hat{g}(\omega) R(\omega), \\ \hat{\mathbf{u}}_T = \begin{pmatrix} -\rho_m \\ -\cos \theta_T / c_m \\ -\sin \theta_T / c_m \end{pmatrix} \exp(-\mathbf{k}_T \cdot (\mathbf{x} - \mathbf{x}_s)) \hat{g}(\omega) T(\omega), \end{cases} \quad (\text{B.1})$$

with \mathbf{k}_I , \mathbf{k}_R and \mathbf{k}_T being the corresponding wavevectors that are of norm ω/c_m and whose direction is normal to the wave fronts. Using the jump conditions in (3) and introducing the

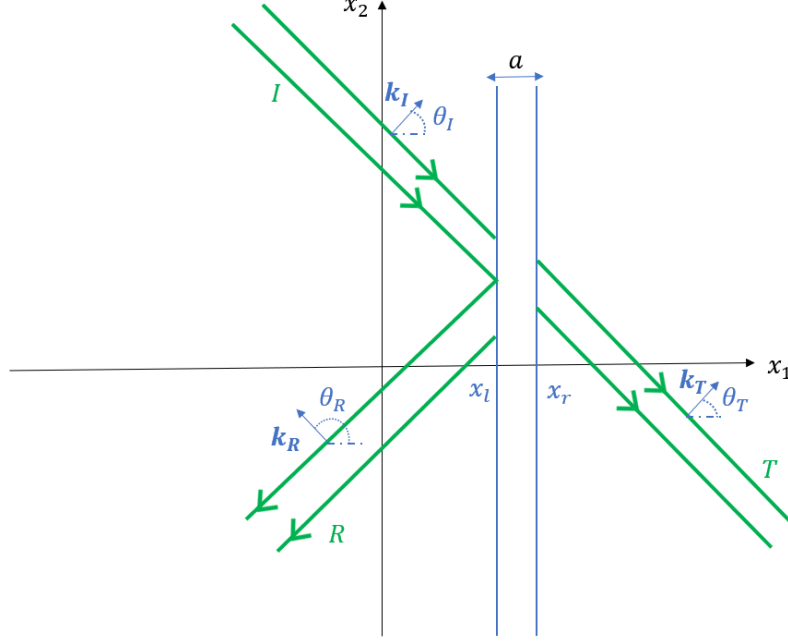


Figure B.13: Incident plane wave (I) illuminating the enlarged interface and leading to reflected (R) and transmitted (T) plane waves.

following parameters

$$\left\{ \begin{array}{l}
 \alpha_1(\omega) = \frac{1}{2c_m^2} \left((C_{11} + h\mathcal{D}(\omega)) \cos(\theta_R)^2 - C_{12} \sin \theta_R \cos \theta_R + (C_{22} + h\mathcal{D}(\omega)) \sin(\theta_R)^2 \right), \\
 \alpha_2(\omega) = \frac{1}{2c_m^2} \left((C_{11} + h\mathcal{D}(\omega)) \cos(\theta_T)^2 - C_{12} \sin \theta_T \cos \theta_T + (C_{22} + h\mathcal{D}(\omega)) \sin(\theta_T)^2 \right), \\
 \alpha_3(\omega) = \frac{1}{2c_m^2} \left((C_{11} + h\mathcal{D}(\omega)) \cos(\theta_I)^2 - C_{12} \sin \theta_I \cos \theta_I + (C_{22} + h\mathcal{D}(\omega)) \sin(\theta_I)^2 \right), \\
 \beta_1 = \frac{\rho_m}{2c_m} (B_1 \cos \theta_R + B_2 \sin \theta_R), \\
 \beta_2 = \frac{\rho_m}{2c_m} (B_1 \cos \theta_T + B_2 \sin \theta_T), \\
 \beta_3 = \frac{\rho_m}{2c_m} (B_1 \cos \theta_I + B_2 \sin \theta_I), \\
 \delta_R(\omega) = \exp \left(i \frac{\omega}{c_m} (x_l \cos \theta_I - x_l \cos \theta_R) \right), \\
 \delta_T(\omega) = \exp \left(i \frac{\omega}{c_m} (x_l \cos \theta_I - x_r \cos \theta_T) \right),
 \end{array} \right. \quad (\text{B.2})$$

then we get the following system concerning the reflected and transmitted waves:

$$\left\{ \begin{array}{l}
 \left(\frac{\cos \theta_R}{c_m} - i\omega \alpha_1 \right) \delta_R(\omega) R(\omega) - \left(\frac{\cos \theta_T}{c_m} + i\omega \alpha_2 \right) \delta_T(\omega) T(\omega) = -\frac{\cos \theta_I}{c_m} + i\omega \alpha_3, \\
 (\rho_m - i\omega \beta_1) \delta_R(\omega) R(\omega) - (\rho_m + i\omega \beta_2) \delta_T(\omega) T(\omega) = -\rho_m + i\omega \beta_3.
 \end{array} \right. \quad (\text{B.3})$$

Introducing the parameters

$$\left\{ \begin{array}{l} Z_1 = \rho_m c_m \cos \theta_I, \\ Z_2 = \rho_m c_m \cos \theta_T, \\ \mathcal{C}_1(\omega) = c_m^2 \left(\rho_m \alpha_1(\omega) + \rho_m \alpha_2(\omega) + \frac{\beta_2}{c_m} \cos \theta_I - \frac{\beta_1}{c_m} \cos \theta_T \right), \\ \mathcal{C}_2(\omega) = c_m^2 \left(-\rho_m \alpha_3(\omega) - \rho_m \alpha_2(\omega) + \frac{\beta_2}{c_m} \cos \theta_I + \frac{\beta_3}{c_m} \cos \theta_T \right), \\ \mathcal{C}_3(\omega) = c_m^2 \left(\rho_m \alpha_1(\omega) - \rho_m \alpha_3(\omega) - \frac{\beta_3}{c_m} \cos \theta_I + \frac{\beta_1}{c_m} \cos \theta_R \right), \\ \mathcal{M}_1(\omega) = c_m^2 (\alpha_2(\omega) \beta_1 - \alpha_1(\omega) \beta_2), \\ \mathcal{M}_2(\omega) = c_m^2 (\alpha_3(\omega) \beta_2 - \alpha_2(\omega) \beta_3), \\ \mathcal{M}_3(\omega) = c_m^2 (\alpha_1(\omega) \beta_3 - \alpha_3(\omega) \beta_1), \end{array} \right. \quad (\text{B.4})$$

we get the reflection coefficient and the transmission coefficient

$$\left\{ \begin{array}{l} R(\omega) = \frac{Z_1 - Z_2 + i\omega \mathcal{C}_2 + \omega^2 \mathcal{M}_2}{Z_1 + Z_2 + i\omega \mathcal{C}_1 + \omega^2 \mathcal{M}_1} \exp \left(-i \frac{\omega}{c_m} (x_l \cos \theta_I - x_l \cos \theta_R) \right), \\ T(\omega) = \frac{2Z_1 + i\omega \mathcal{C}_3 + \omega^2 \mathcal{M}_3}{Z_1 + Z_2 + i\omega \mathcal{C}_1 + \omega^2 \mathcal{M}_1} \exp \left(-i \frac{\omega}{c_m} (x_l \cos \theta_I - x_r \cos \theta_T) \right), \end{array} \right. \quad (\text{B.5})$$

with $\theta_R = \pi/2 + \theta_I$ and $\theta_T = \theta_I$. These expressions used in (B.1) give the sought expression for $\hat{\mathbf{u}}(\mathbf{x}, \omega)$. An inverse discrete Fourier transform in time provides the semi-analytical time-domain solution considered in Section 5. It can be shown that the 1D semi-analytical solution is recovered when setting $\theta_I = 0$, $x_2 = 0$ and $v_2 = 0$ in the 2D solution.

Remark 7. *When the enlarged interface is tilted of an angle $-\phi$ with the horizontal axis then the calculation of the associated scattering coefficients follows the same lines in the rotated coordinate system $(\zeta, \eta) = (\cos \phi x_1 - \sin \phi x_2, \sin \phi x_1 + \cos \phi x_2)$. A rotation of angle $-\phi$ is then necessary after the inverse discrete Fourier transform to express the vectorial field \mathbf{v} in the basis (x_1, x_2) .*

Appendix C. Semi-analytical solution for a plane wave on a circular interface

We consider an incident plane wave at an angle θ_I with the horizontal axis and an enlarged circular interface defined by two circles of centers (x_c, y_c) and radii a^- and a^+ , with $a^- > a^+$. The initial conditions are given in (47). The approach presented here applies to the particular interface parameter values $B_2 = C_{12} = \alpha_0 = 0$, the other parameters being arbitrary. The method employed in [14] for fluid-solid circular interface is applied here: to calculate the solution, we consider its frequency-domain formulation (3). The wavefield solution $\hat{\mathbf{u}}(\mathbf{x}, \omega)$ is then decomposed into incident, reflected and transmitted waves. They are written on a truncated basis of Bessel functions using the Jacobi-Anger decomposition and the associated

diffraction coefficients are derived from the jump conditions. We start by introducing the harmonic acoustic potential $\hat{\Phi}$ such that

$$\hat{p} = -i\omega \rho_m \hat{\Phi}, \quad \hat{v}_\nu = \partial_r \hat{\Phi}, \quad \hat{v}_\tau = \frac{1}{r} \partial_\phi \hat{\Phi}. \quad (\text{C.1})$$

The harmonic potential of the incident plane wave is:

$$\hat{\Phi}_I(x_1, x_2, \omega) = \exp\left(-\frac{i\omega}{c_m} (x_1 \cos \theta_I + x_2 \sin \theta_I)\right) \frac{\hat{g}(\omega)}{i\omega}. \quad (\text{C.2})$$

We introduce a polar coordinates system (r, ϕ) such as $x_1 = x_c + r \cos \phi$ and $x_2 = y_c + r \sin \phi$, so the above potential reads:

$$\hat{\Phi}_I(x_1, x_2, \omega) = FS \exp(-ikr \cos \alpha), \quad (\text{C.3})$$

with $F = \hat{g}(\omega)/i\omega$, $S = \exp(-ik(x_c \cos \theta_I + y_c \sin \theta_I))$, $\alpha = \phi - \theta_I$ and $k = \omega/c_m$. The Bessel functions of the first-kind \mathcal{J}_n satisfy the Jacobi–Anger expansion, see e.g. [10]:

$$\exp(-ir \cos \alpha) = \sum_{n=0}^{\infty} \epsilon_n (-i)^n \cos(n\alpha) \mathcal{J}_n(r), \quad (\text{C.4})$$

with $\epsilon_n = 1$ if $n = 0, 2$ else. From (C.3) and (C.4), we therefore express the potential $\hat{\Phi}_I$ as:

$$\hat{\Phi}_I(x_1, x_2, \omega) = FS \sum_{n=0}^{\infty} \epsilon_n (-i)^n \cos(n\alpha) \mathcal{J}_n(kr). \quad (\text{C.5})$$

To satisfy the Sommerfeld condition, which is satisfied by the radiated wavefield at infinity in the classical acoustic medium, the harmonic acoustic potential $\hat{\Phi}_R$ of the reflected wave is written on the basis of Hankel functions of the second-kind \mathcal{H}_n . To prevent singularities from occurring at $r = 0$, the harmonic potential $\hat{\Phi}_T$ of transmitted waves is written on the basis of the Bessel functions of the first-kind, i.e.

$$\hat{\Phi}_R(x_1, x_2, \omega) = \sum_{n=0}^{\infty} R_n \cos(n\alpha) \mathcal{H}_n(kr), \quad \hat{\Phi}_T(x_1, x_2, \omega) = \sum_{n=0}^{\infty} T_n \cos(n\alpha) \mathcal{J}_n(kr), \quad (\text{C.6})$$

where R_n and T_n are the coefficients of reflexion and transmission that have to be determined. The velocity $\hat{v} = (\hat{v}_\nu, \hat{v}_\tau)^\top$ and the pressure \hat{p} fields are deduced from the potential $\hat{\Phi}$ using (C.3). From (C.1), (C.5) and (C.6), we deduce the components of the incident, reflected and

transmitted waves as follows:

$$\begin{cases}
\hat{p}_I = -i\omega \rho_m FS \sum_{n=0}^{\infty} \epsilon_n (-i)^n \cos(n\alpha) \mathcal{J}_n(kr), \\
\hat{v}_{I\nu} = k FS \sum_{n=0}^{\infty} \epsilon_n (-i)^n \cos(n\alpha) \mathcal{J}'_n(kr), \\
\hat{v}_{I\tau} = -\frac{1}{r} FS \sum_{n=0}^{\infty} \epsilon_n (-i)^n n \sin(n\alpha) \mathcal{J}_n(kr), \\
\hat{p}_R = -i\omega \rho_m \sum_{n=0}^{\infty} R_n \cos(n\alpha) \mathcal{H}_n(kr), \\
\hat{v}_{R\nu} = k \sum_{n=0}^{\infty} R_n \cos(n\alpha) \mathcal{H}'_n(kr), \\
\hat{v}_{R\tau} = -\frac{1}{r} \sum_{n=0}^{\infty} R_n n \sin(n\alpha) \mathcal{H}_n(kr), \\
\hat{p}_T = -i\omega \rho_m \sum_{n=0}^{\infty} T_n \cos(n\alpha) \mathcal{J}_n(kr), \\
\hat{v}_{T\nu} = k \sum_{n=0}^{\infty} T_n \cos(n\alpha) \mathcal{J}'_n(kr), \\
\hat{v}_{T\tau} = -\frac{1}{r} \sum_{n=0}^{\infty} T_n n \sin(n\alpha) \mathcal{J}_n(kr).
\end{cases} \tag{C.7}$$

In the case where $B_2 = C_{12} = \alpha_0 = 0$ an identification is possible, then the coefficients R_n and T_n are deduced from the jump conditions in (44), which for all $0 \leq \phi \leq 2\pi$ read:

$$\hat{p}_T(a^+, \phi) - (\hat{p}_I + \hat{p}_R)(a^-, \phi) = \frac{B_1}{2} (\partial_r \hat{p}_T(a^+, \phi) + (\partial_r \hat{p}_I + \partial_r \hat{p}_R)(a^-, \phi)),$$

and

$$\begin{aligned}
\hat{v}_{T\nu}(a^+, \phi) - (\hat{v}_{I\nu} + \hat{v}_{R\nu})(a^-, \phi) &= \frac{C_{11}}{2} (\partial_r \hat{v}_{T\nu}(a^+, \phi) + (\partial_r \hat{v}_{I\nu} + \partial_r \hat{v}_{R\nu})(a^-, \phi)) \\
&+ \frac{C_{22}}{2} \left(\frac{1}{a^+} \partial_\phi \hat{v}_{T\tau}(a^+, \phi) + \frac{1}{a^-} (\partial_\phi \hat{v}_{I\tau} + \partial_\phi \hat{v}_{R\tau})(a^-, \phi) \right), \\
&+ \frac{k^2 h \mathcal{D}(\omega)}{2} (\hat{p}_T(a^+, \phi) + (\hat{p}_I + \hat{p}_R)(a^-, \phi)).
\end{aligned}$$

From there, one obtains the following system satisfied by the coefficients R_n and T_n for all $n \geq 0$:

$$\left\{ \begin{array}{l} [k\mathcal{J}'_n(ka^+) - \frac{C_{11}}{2}k^2\mathcal{J}''_n(ka^+) + \frac{C_{22}}{2}\left(\frac{n}{a^+}\right)^2\mathcal{J}_n(ka^+) - k^2\frac{h}{2}\mathcal{D}(\omega)\mathcal{J}_n(ka^+)]T_n \\ + [-k\mathcal{H}'_n(ka^-) - \frac{C_{11}}{2}k^2\mathcal{H}''_n(ka^-) + \frac{C_{22}}{2}\left(\frac{n}{a^-}\right)^2\mathcal{H}_n(ka^-) - k^2\frac{h}{2}\mathcal{D}(\omega)\mathcal{H}_n(ka^-)]R_n \\ = FS\epsilon_n(-i)^n[k\mathcal{J}'_n(ka^-) + \frac{C_{11}}{2}k^2\mathcal{J}''_n(ka^-) - \frac{C_{22}}{2}\left(\frac{n}{a^-}\right)^2\mathcal{J}_n(ka^-) + k^2\frac{h}{2}\mathcal{D}(\omega)\mathcal{J}_n(ka^-)], \\ \\ [\mathcal{J}_n(ka^+) - \frac{B_1}{2}k\mathcal{J}'_n(ka^+)]T_n + [-\mathcal{H}_n(ka^-) - \frac{B_1}{2}k\mathcal{H}'_n(ka^-)]R_n \\ = FS\epsilon_n(-i)^n[\mathcal{J}_n(ka^-) + \frac{B_1}{2}k\mathcal{J}'_n(ka^-)]. \end{array} \right. \quad (\text{C.8})$$

In practice, one considers a finite number N_{Bessel} of modes. The coefficients R_n and T_n are computed from the associated systems (C.8) and (C.7) is finally used to obtain the wavefield solution $\hat{\mathbf{u}}(\mathbf{x}, \omega)$ in the frequency domain. A discrete inverse Fourier transform in time yields the semi-analytical solution considered in Section 5.2.3.

References

- [1] C. Bellis and B. Lombard. Simulating transient wave phenomena in acoustic metamaterials using auxiliary fields. *Wave Motion*, 86:175–194, March 2019.
- [2] A. Bensoussan, J.-L. Lions, and G. Papanicolaou. *Asymptotic Analysis for Periodic Structures*. North-Holland, 1978.
- [3] M. Bonnet, R. Cornaggia, and B. Guzina. Microstructural topological sensitivities of the second-order macroscopic model for waves in periodic media. *SIAM Journal on Applied Mathematics*, 78(4):2057–2082, jan 2018.
- [4] A. Bonnet-Bendhia, D. Drissi, and N. Gmati. Simulation of a muffler’s transmission losses by a homogenized finite element method. *Journal of Computational Acoustics*, 12(3):447–474, 2004.
- [5] M. Cassier, P. Joly, and M. Kachanovska. Mathematical models for dispersive electromagnetic waves: An overview. *Computers & Mathematics with Applications*, 74(11):2792–2830, 2017.
- [6] G. Chiavassa and B. Lombard. Time domain numerical modeling of wave propagation in 2D heterogeneous porous media. *Journal of Computational Physics*, 230(13):5288–5309, jun 2011.
- [7] M. David, C. Pideri, and J.-J. Marigo. Homogenized interface model describing inhomogeneities located on a surface. *Journal of Elasticity*, 109(2):153–187, 2012.

- [8] B. Delourme. *Modèles asymptotiques des interfaces fines et périodiques en électromagnétisme*. PhD Thesis - Université Pierre et Marie Curie - Paris VI, 2010.
- [9] B. Guzina and M. Bonnet. Small-inclusion asymptotic of misfit functionals for inverse problems in acoustics. *Inverse Problems*, 22(5):1761–1785, sep 2006.
- [10] R. B. Harvey, P. M. Morse, and H. Feschbach. Methods of theoretical physics. *The Mathematical Gazette*, 39(327):80, feb 1955.
- [11] B. Lombard. *Modélisation numérique de la propagation et de la diffraction d’ondes mécaniques*. Habilitation à Diriger des Recherches de l’Université Aix-Marseille 2, 2010.
- [12] B. Lombard, A. Maurel, and J.-J. Marigo. Numerical modeling of the acoustic wave propagation across an homogenized rigid microstructure in the time domain. *Journal of Computational Physics*, 335:558–577, 2017.
- [13] B. Lombard and J. Piraux. How to incorporate the spring-mass conditions in finite-difference schemes. *SIAM Journal of Scientific Computing*, 24(4):1379–1407, 2003.
- [14] B. Lombard and J. Piraux. Numerical treatment of two-dimensional interfaces for acoustic and elastic waves. *Journal of Computational Physics*, 195(1):90–116, mar 2004.
- [15] B. Lombard and J. Piraux. Numerical modeling of elastic waves across imperfect contacts. *SIAM Journal on Scientific Computing*, 28(1):172–205, jan 2006.
- [16] B. Lombard, J. Piraux, C. Gélis, and J. Virieux. Free and smooth boundaries in 2-d finite-difference schemes for transient elastic waves. *Geophysical Journal International*, 172(1):252–261, jan 2008.
- [17] F. Lorcher and C.-D. Munz. Lax-wendroff-type schemes of arbitrary order in several space dimensions. *IMA Journal of Numerical Analysis*, 27(3):593–615, nov 2006.
- [18] G. Ma, M. Yang, S. Xiao, Z. Yang, and P. Sheng. Acoustic metasurface with hybrid resonances. *Nature Materials*, 13:873–879, 2014.
- [19] J.-J. Marigo and A. Maurel. Homogenization models for thin rigid structured surfaces and films. *The Journal of the Acoustical Society of America*, 140(1):260–273, 2016.
- [20] J.-J. Marigo, A. Maurel, K. Pham, and A. Sbitti. Effective dynamic properties of a row of elastic inclusions: The case of scalar shear waves. *Journal of Elasticity*, 128(2):265–289, 2017.
- [21] J.-J. Marigo and C. Pideri. The effective behaviour of elastic bodies containing microcracks or microholes localized on a surface. *International Journal of Damage Mechanics, SAGE Publications*, 20:1151–1177, 2011.
- [22] K. Pham, A. Maurel, and J.-J. Marigo. Two scale homogenization of a row of locally resonant inclusions - the case of shear waves. *Journal of the Mechanics and Physics of Solids*, 106:80–94, 2017.

- [23] J. Sanchez-Hubert and E. Sanchez-Palencia. *Introduction aux Méthodes Asymptotiques et à l'Homogénéisation*. Collection Mathématiques Appliquées pour la Maîtrise, 1992.
- [24] L. Schwan, O. Umnova, and C. Boutin. Sound absorption and reflection from a resonant metasurface: Homogenisation model with experimental validation. *Wave Motion*, 72:154–172, 2017.
- [25] T. Schwartzkopff, M. Dumbser, and C.-D. Munz. Fast high order ADER schemes for linear hyperbolic equations. *Journal of Computational Physics*, 197(2):532–539, jul 2004.
- [26] X. Su, Z. Lu, and A.N. Norris. Elastic metasurfaces for splitting sv- and p-waves in elastic solids. *Journal of Applied Physics*, 123:091701, 2018.
- [27] W. T. Vetterling W. H. Press, S. A. Teukolskyn and B. P. Flannery. *Numerical Recipes in C: The Art of Scientific Computing*. Cambridge University Press, 1992.
- [28] C. Zhang and R. J. LeVeque. The immersed interface method for acoustic wave equations with discontinuous coefficients. *Wave Motion*, 25:237–263, 1997.